ALMA MATER STUDIORUM · UNIVERSITÀ DI BOLOGNA

Dipartimento di Fisica e Astronomia
Corso di Laurea Magistrale in Astrofisica e Cosmologia

Density and Velocity Profiles in Dark Scattering Models

Tesi di Laurea

Presentata da:
Beatrice D'Angelo

Relatore:
Chiar.mo Prof. Lauro Moscardini

Correlatore:
Dott. Marco Baldi

Correlatore:
Dott. Carlo Giocoli

Appello I
Anno Accademico 2017-2018

Contents

Abstract

One of the most intriguing issues in modern physics lies on the mystery surrounding the true nature of Dark Energy. Although observational cosmology is living in an era of unprecedented precision, as CMB, BAO, and Supernovae Ia measurements seem to be in a very good agreement with the predictions of the standard model, Planck data show a tension with the low redshift ones such as cluster counts and weak lensing data, which point towards a lower rate of structure growth. A possible explanation of this behaviour is that ΛCDM is not the correct model describing the evolution of the Universe. Finding an alternative model capable of providing a higher accuracy is strongly fostered because of the two most pressing problems related to the standard model: *fine tuning* and *coincidence*, both associated with the cosmological constant.

Some of the properties of the two constituents of the dark sector are still unknown and the fact that they are considered uncoupled is just an assumption. Many models of Coupled Dark Energy are studied in the literature, however the vast majority of them involve an energy exchange between the two fluids, with a far smaller degree of momentum exchange. In the former case, both the expansion history and the growth of structures are modified, while models based on pure momentum transfer theory leave the background cosmology unaltered, and consequently fewer observational signatures.

Dark Scattering models feature an evolution of a classic scalar field ϕ playing the role of DE, and an interaction between DM particles and this field. Given the low DE density and the non-relativistic velocity associated with CDM particles, elastic scattering has been chosen as the simplest and most natural kind of interaction, leading to a model characterized by a pure momentum exchange between them.

Considering CDM particles moving through the DE fluid, they would observe a nonzero momentum flux, which imparts a force proportional to the CDM-DE scattering cross section.

This thesis project is the analysis of data from CDM-only cosmological N-body simulations with a modified version of GADGET which implements the drag force related to the DE-CDM momentum exchange, with the aim to find evidence that could allow to distinguish between standard model and cDE ones. Many properties of halos have been studied in the past years, here the analysis is focused on the velocity fields, where CDM-DE cross-section can leave observational signatures.

These simulations involved five cosmological models, namely two models with a time-dependent equation of state parameter $w(a)$, two wCDM models ($w = -0.9$ and $w = -1.1$), and the reference ΛCDM cosmology ($w = -1$), and all of them started from the same initial conditions, so that each difference

detected among the outputs could be ascribed to the effects of the different models.

The results of the study consist in a series of plots showing density and, for the first time on these data, velocity profiles of a significant number of dark matter halos for each cosmology, divided into mass bins and for three redshifts $z = 0$, $z = 0.5$ e $z = 1$.

The mass bins chosen are $6 \cdot 10^{13} < \frac{M}{M\odot} < 2 \cdot 10^{14}$ (galaxy-halos), $2 \cdot 10^{14} < \frac{M}{M\odot} < 6 \cdot 10^{14}$ (group-halos), $6 \cdot 10^{14} < \frac{M}{M\odot} < 3 \cdot 10^{15}$ (cluster-halos).

Dark Scattering Models are expected to alter the collapse and virialisation process of gravitationally bound systems, as the effect of a friction term results in two opposite trends. In the linear regime, particles are far from the halo and their direction of motion is radial. As they fall into the potential well of the halo, the friction term acts in the same direction of the gravitational acceleration, slowing down the particles. Conversely, in the nonlinear regime (i.e. near to the centre of the halo) the collapsing structures start to gain angular moment and particles a tangential direction of motion leading to a loss of kinetic energy, and consequently a faster collapse.

Therefore, halos simulated with dark scattering models are expected to show a suppression in the growth of structures in the linear regime, while in the nonlinear regime the extra friction should lead to a faster collapse and virialisation, and therefore these halos should form earlier.

For this reason, possible evidence of lower velocities in the outer regions with a mild recovery on small scales is researched in dark matter halos velocity profiles of the dark scattering models under investigation.

Sommario

I modelli Dark Scattering sono stati sviluppati nell'ambito delle teorie cosmologiche non standard, per rispondere agli interrogativi ancora aperti che il modello ΛCDM presenta. Per quanto la cosmologia osservativa odierna sia in una fase di precisione senza precedenti, con i dati CMB, BAO, e Supernovae Ia che mostrano di essere in accordo con l'attuale modello standard, i dati Planck sono in tensione con quelli a basso redshift, provenienti ad esempio dal misurazioni di weak lensing, che puntano verso un tasso più basso di crescita delle strutture. Tale attrito può derivare dalla incorretta assunzione che ΛCDM sia il modello adatto a descrivere l'evoluzione dell'Universo. La ricerca di modelli alternativi che possano fornire una maggior accuratezza è fortemente motivata dai due problemi principali legati al modello standard: il fine tuning e la coincidenza, entrambi associati alla costante cosmologica.

I modelli Dark Scattering qui trattati sono caratterizzati dalla evoluzione di un campo scalare classico ϕ con il ruolo di Energia Oscura (DE), e dalla interazione che le particelle di Materia Oscura (DM) hanno con questo campo. Date la bassa densità dell'energia oscura e la velocità non relativistica associata alle particelle DM, è stato scelto lo scattering elastico per questo tipo di interazione. Considerando le particelle DM in moto attraverso il fluido DE, esse osservano un flusso di momento diverso da zero, indice di una forza proporzionale alla sezione d'urto di scattering tra DE e DM.

Nel presente lavoro sono stati analizzati dati provenienti da simulazioni cosmologiche N-body DM-only per cinque modelli: due a equazione di stato DE costante ($w = -0.9$ e $w = -1.1$), due con equazione di stato dipendente dal tempo $w(a)$, e infine il modello standard ΛCDM come base di confronto. Le condizioni iniziali sono uguali per tutti i modelli, in modo tale che ogni differenza rilevata nei risultati sia riconducibile agli effetti dei diversi modelli cosmologici.

Sono stati ricavati i profili di densità e, per la prima volta su questi dati, i profili di velocità, di un centinaio di aloni di materia oscura per ogni cosmologia, divisi in bin di massa e per tre redshift $z = 0$, $z = 0.5$ e $z = 1$.

I bin di massa scelti sono $6 \cdot 10^{13} < \frac{M}{M\odot} < 2 \cdot 10^{14}$ (aloni DM galattici), $2 \cdot 10^{14} < \frac{M}{M\odot} < 6 \cdot 10^{14}$ (aloni DM attorno a gruppi), $6 \cdot 10^{14} < \frac{M}{M\odot} < 3 \cdot 10^{15}$ (aloni di ammassi).

Viene evidenziato come il termine aggiuntivo di drag nei modelli dark scattering abbia due effetti diversi nella crescita delle strutture. Nel regime lineare, infatti, le particelle DM in infall verso il centro degli ammassi hanno una direzione radiale del moto e l'attrito con il fluido DE le fa rallentare, diminuendo la loro velocità. Quando passano al regime non lineare, acquistano una componente tangenziale di velocità che di fatto fa sì che l'interazione con l'energia

oscura provochi una perdita di energia cinetica con conseguente collasso più rapido. Per questo motivo nei profili di velocità creati si cerca l'evidenza di questo effetto, che risulta in una soppressione della crescita per le regioni esterne con un recupero nelle scale più piccole, riscontrabile nei grafici.

Chapter 1

Basic Concepts and Standard Model

1.1 FRW Background

The most important force in the Universe is gravity, as it is the strongest force acting on long distance. This is why General Relativity plays a crucial role in describing the physical properties of the Universe.

From Special Relativity, the distance between two events at coordinates $(x,\ y,\ z,\ t)$ and $(x+\mathrm{d}x,\ y+\mathrm{d}y,\ z+\mathrm{d}z,\ t+\mathrm{d}t)$ can be written as

$$\mathrm{d}s^2 = c^2\,\mathrm{d}t^2 - (\mathrm{d}x^2 + \mathrm{d}y^2 + \mathrm{d}z^2),$$

where $\mathrm{d}s$ is invariant under a coordinate system change and photons move on geodesics for which $\mathrm{d}s = 0$.

This equation can be generalized in the case of a non-flat spacetime: using General Relativity, an interval between two events is defined by

$$\mathrm{d}s^2 = g_{ij}\,\mathrm{d}x^i\,\mathrm{d}x^j,$$

with i and j running from 0 to 3: x^1, x^2, and x^3 are space coordinates and c^2x^0 is the time coordinate.

According to the Cosmological Principle, no direction is preferred, which means that the Universe is homogeneous and isotropic on large scales. For this reason, one can define a *proper time* such that the spatial metric is identical in all directions. Therefore, g_{0i} must be equal to zero, and the metric takes the form

$$\mathrm{d}s^2 = c^2\,\mathrm{d}t^2 + g_{ij}\,\mathrm{d}x^i\,\mathrm{d}x^j = c^2\,\mathrm{d}t^2 - \mathrm{d}l^2,$$

where the interval is only spatial. This is the most common way to split the metric into the spatial and temporal components.

In order to find a general equation for $\mathrm{d}l^2$, it is useful to consider first the simple case of a two-dimensional space. Such a space can be either flat (infinite curvature radius R), a spherical surface with $R > 0$, or a hyperbolic surface with $R < 0$.

For the first case, polar coordinates can be used

$$\mathrm{d}l^2 = \mathrm{d}x^2 + \mathrm{d}y^2 = \mathrm{d}\rho^2 + \rho^2\,\mathrm{d}\phi^2,$$

where $0 \leq \rho < \infty$ and $0 \leq \phi < 2\pi$.

If we introduce $r \equiv \rho/a$, running from $0 \leq r < \infty$, with $[a] = [L]$, the equation becomes

$$\mathrm{d}l^2 = a^2(\mathrm{d}r^2 + r^2\,\mathrm{d}\phi^2).$$

If the space has a spherical curvature, spherical coordinates ($0 \leq \theta \leq \pi$ and $0 \leq \phi < 2\pi$) lead to

$$\mathrm{d}l^2 = R^2(\sin^2\theta\,\mathrm{d}\phi^2 + \mathrm{d}\theta^2) = a^2\left(\frac{\mathrm{d}r^2}{1-r^2} + r^2\,\mathrm{d}\phi^2\right),$$

having set $R \equiv a$ and $r \equiv \sin\theta \implies \mathrm{d}r = \cos\theta\,\mathrm{d}\theta$.

On the surface of a hyperboloid, the metric is given by

$$\mathrm{d}l^2 = R^2(\sinh^2\theta\,\mathrm{d}\phi^2 + \mathrm{d}\theta^2) = a^2\left(\frac{\mathrm{d}r^2}{1+r^2} + r^2\,\mathrm{d}\phi^2\right)$$

where $r \equiv \sinh\theta$ and $R \equiv a$.

Interestingly, the three equations share a quite similar form, so that we can write

$$\mathrm{d}l^2 = a^2\left(\frac{\mathrm{d}r^2}{1-kr^2} + r^2\,\mathrm{d}\phi^2\right).$$

k is the *curvature parameter*: if $k = 0$ the space is flat, if $k = +1$ is spherical, and if $k = -1$ is hyperbolic.

The three-dimensional generalization of this formula is obtained by substituting $\mathrm{d}\phi^2$ with $\mathrm{d}\Omega^2 = \mathrm{d}\theta^2 + \sin^2\theta\,\mathrm{d}\phi^2$ and it is called the **Friedmann-Robertson-Walker Metric**:

$$\mathrm{d}l^2 = (c\,\mathrm{d}t)^2 - a^2(t)\left[\frac{\mathrm{d}r^2}{1-kr^2} + r^2(\sin^2\theta\,\mathrm{d}\phi^2 + \mathrm{d}\theta^2)\right],$$

where r, θ, and ϕ are the comoving coordinates (with r dimensionless), t is the proper time, and $a = a(t)$ is called the *cosmic scale factor* or the *expansion parameter*, it can be time dependent and in general has $[a(t)] = [cm^2]$.

One of the main goals of cosmology is to determine the value of k, which is associated with the matter and energy density content of the Universe.

1.1.1 Friedmann Equations

Einstein's General Relativity changed the classical description of gravity being a force between bodies, and from 1916 gravity started to be seen as a property of spacetime, namely the observed effect of the warping of spacetime caused by massive objects.

In order to link matter content and curvature of space, Einstein developed the so called *Einstein's field equations*, which represent the formal definition of General Relativity Theory

$$G_{ij} \equiv R_{ij} - \frac{1}{2}Rg_{ij} = \frac{8\pi G}{c^4}T_{ij}. \qquad (1.1.1)$$

G_{ij} is the Einstein's tensor expressing the curvature, T_{ij} is the stress-energy tensor describing the matter distribution, and for a perfect fluid with pressure p and energy density ρ it takes the form

$$T_{ij} = -pg_{ij} + (p + \rho c^2)u_i u_j, \tag{1.1.2}$$

with u_i being the fluid four-velocity

$$u_i = g_{ij}u^j = g_{ij}\frac{\mathrm{d}x^j}{\mathrm{d}s},$$

and $x^j(s)$ is the world line of the fluid element, namely its trajectory.

Conservation laws of mass, energy, and momentum which play a key-role are defined in special relativity by

$$\frac{\partial T_{ij}}{\partial x^j} = 0,$$

and in GR the analogous equation is obtained by using the covariant derivative

$$T_i{}^j{}_{;j} = 0.$$

The quantity $8\pi G/c^4$ of (1.1.1) ensures that the limit of weak gravitational field ($\phi/c \ll 1$) and non-relativistic source of gravity ($p \ll \rho c^2$) result in the classical Poisson's equation

$$\nabla^2\phi = 4\pi G\rho.$$

In the case of a relativistic fluid we must drop the assumption $p \ll \rho c^2$ and thus we can take the field equations in order to obtain a modified Poisson equation

$$\nabla^2\phi = 4\pi G\left(\rho + \frac{3p}{c^2}\right). \tag{1.1.3}$$

The above equation clearly shows that a negative pressure arising from $c^2\rho + 3p < 0$ would produce a *repulsive* gravitational force.

In 1922, the mathematician Alexander Friedmann derived a set of equations with the aim of characterizing the evolution of the Universe under certain assumptions. If the Cosmological Principle is accepted, i.e if we take the FRW metric, and using the energy-momentum tensor of a perfect fluid (1.1.2), Friedmann demonstrated that Einstein's equations yield

$$\ddot{a} = -\frac{4\pi}{3}G\left(\rho + \frac{3p}{c^2}\right)a \tag{1.1.4}$$

$$\dot{a}^2 + kc^2 = \frac{8\pi}{3}G\rho a^2. \tag{1.1.5}$$

Solutions of the Friedmann equations lead to different Friedmann Models depending on the choices of k, ρ, and p.

We can exploit the equation of adiabatic expansion of the Universe, which states that the Universe does not exchange heat during its expansion,

$$\mathrm{d}(\rho c^2 a^3) = -p\,\mathrm{d}a^3$$

and rewrite (1.1.5) for $a = a_0$, $\rho = \rho_0$ (where the subscript 0 represents the present time)

$$\left(\frac{\dot{a}}{a_0}\right)^2 + \frac{kc^2}{a_0^2} = \frac{8\pi}{3a_0^2} G\rho_0 a_0^2 \implies H_0^2 \left(1 - \frac{\rho_0}{\rho_{0,crit}}\right) = -\frac{kc^2}{a_0^2} \tag{1.1.6}$$

where $H_0 \equiv \dot{a}/a_0$ is the Hubble parameter at present time, ρ_{crit} is called *Critical Density* and it is defined at $t = t_0$ by

$$\rho_{0,crit} := \frac{3H_0^2}{8\pi G}.$$

It represents the ratio between expansion and gravity, thus its value determines the fate of the Universe, whether it is gravity dominated ($\rho > \rho_{0,crit}$), or expansion dominated ($\rho_0 < \rho_{0,crit}$).

From (1.1.6) we can see that:

$$\begin{aligned} k = \quad -1 &\implies \rho_0 < \rho_{0,crit} \\ k = \quad 0 &\implies \rho_0 = \rho_{0,crit} \\ k = \quad +1 &\implies \rho_0 > \rho_{0,crit}. \end{aligned}$$

Let's introduce the *Density Parameter*

$$\Omega := \frac{\rho}{\rho_{crit}}, \tag{1.1.7}$$

which allows us to rewrite (1.1.6) in a more generic form

$$\left(\frac{\dot{a}}{a_0}\right)^2 = H_0^2 \left[\Omega_0 \left(\frac{a_0}{a}\right)^{1+3w} + (1 - \Omega_0)\right]. \tag{1.1.8}$$

w represents the relationship between density and pressure of a fluid, which is expressed by an equation of state, i.e. something of the form $p = p(\rho)$. In general, we can write

$$p = w\rho c^2,$$

where w is a constant lying in the range $[0, 1]$ (the so-called *Zel'dovich interval*) for a vast number of models.

w is also associated with the adiabatic sound speed of the fluid, since

$$c_s = \left(\frac{\partial p}{\partial \rho}\right)_S^{1/2} = c\sqrt{w}.$$

It appears clear that, in order to avoid the cases of $c_s > c$ and negative radicand, w must be both < 1 and > 0, although we will show later that these assumptions can be violated under some circumstances.

From (1.1.8), we can point up the equation for the evolution of the Hubble parameter

$$H^2(t) = H_0^2 \left(\frac{a_0}{a}\right)^2 \left[\Omega_0 \left(\frac{a_0}{a}\right)^{1+3w} + (1-\Omega_0)\right],$$

so that

$$\begin{aligned} k = & -1 \implies \Omega_0 < 1, \\ k = & \;\;\;0 \implies \Omega_0 = 1, \\ k = & +1 \implies \Omega_0 > 1. \end{aligned}$$

Today's value of H is far from being well known, best estimates give

$$H_0 = h \cdot 100 \ \text{km/s} \cdot \text{Mpc} \qquad \text{with } h \simeq 0.7$$

which in turns leads to

$$\rho_{0,crit} = 1.9 \cdot 10^{-29} h^2 \ \text{g/cm}^3 = 2.775 \cdot 10^{11} h^2 M_\odot/\text{Mpc}^3.$$

The most important achievement of Friedmann's equations is the evidence of non-stationarity of the Universe: in order to have a static Universe we should put $\dot{a} \equiv \ddot{a} \equiv 0$, and consequently from (1.1.4) we are left with

$$\rho = -\frac{3p}{c^2},$$

but ρ and p cannot have opposite sign, as they are both positive.

This problem drove Einstein to modify his equations in 1917, inserting a constant with the aim of maintaining the stationarity

$$R_{ij} - \frac{1}{2}R g_{ij} - \Lambda g_{ij} = \frac{8\pi G}{c^4} T_{ij}. \tag{1.1.9}$$

Λ is the *cosmological constant* and represents the curvature of empty space. If we move the Λ term on the right side of (1.1.9) we obtain the stress-energy tensor of the vacuum

$$T^{ij}_{\text{vac}} = \frac{\Lambda c^4}{8\pi G} g^{ij}. \tag{1.1.10}$$

1.1.2 Cosmological Models

Generally speaking, the evolution of density depends of the equation of state parameter w, according to the equation of adiabatic expansion

$$\begin{aligned} \mathrm{d}(\rho c^2 a^3) = -p\,\mathrm{d}a^3 = -w\rho c^2\,\mathrm{d}a &\implies a^3\,\mathrm{d}\rho + 3\rho a^2\,\mathrm{d}a = -3w\rho a^2\,\mathrm{d}a \\ &\implies a^3\,\mathrm{d}\rho = -3a^2\rho(1+w)\,\mathrm{d}a \\ &\implies \frac{\mathrm{d}\rho}{\rho} = -3(1+w)\frac{\mathrm{d}a}{a} \\ &\implies \rho \propto a^{-3(1+w)} \end{aligned} \tag{1.1.11}$$

If $w = 0$ pressure is negligible, and the Universe is made of *dust*, which is a good approximation to non-relativistic fluid. In fact, if we take the ideal gas law

$$p = nK_BT = \frac{\rho_M}{m_p}K_BT,$$

where n is the number density, T is the absolute temperature, and K_B is the Boltzmann constant

$$K_B = 1.38 \cdot 10^{-16}\ \text{erg/K},$$

thermal energy K_BT is considerably smaller than particles rest mass m_p, thus $w \simeq 0$.

On the other hand, a *radiative* fluid characterized by non-degenerate, relativistic particles ($w = 1/3$) has pressure and density related by

$$p = \frac{1}{3}\rho c^2.$$

As for the equation of state of vacuum, the energy-momentum tensor derived in (1.1.10) must be the same for all observers since there is no preferred direction, and this is equivalent to saying that it does not have to change for Lorentz transformations. Therefore, T^{ij} has to be proportional to the metric tensor, which is the only isotropic rank 2 tensor apart from zero, so that the vacuum equation of state takes the form of

$$p = -\rho c^2,$$

with $w = -1$.

The importance of vacuum energy appears now clear: a positive Λ leads to a large-scale repulsion. Vacuum energy is a constant and it acts as a reservoir of unlimited energy.

From (1.1.11), we can easily derive the equations for the evolution of the three components of the energy content of the Universe, namely matter ($w = 0$), radiation ($w = 1/3$), and cosmological constant ($w = -1$).

$$\begin{aligned} \rho_M &= \rho_{0,M}\left(\frac{a_0}{a}\right)^3, \\ \rho_R &= \rho_{0,R}\left(\frac{a_0}{a}\right)^4, \\ \rho_\Lambda &= \rho_{0,\Lambda}\left(\frac{a_0}{a}\right)^0 = \rho_{0,\Lambda}. \end{aligned} \tag{1.1.12}$$

Recent measurements (Planck 2015 [1]) provide

$$\begin{aligned} &\rho_{0,M} \simeq 0.3\rho_{0,crit} &&\Longrightarrow \Omega_{0,M} \simeq 0.3, \\ &\rho_{0,R} \simeq 10^{-34}\,\text{g/cm}^3 &&\Longrightarrow \Omega_{0,R} \simeq 10^{-5}, \\ &\rho_{0,\Lambda} \simeq 0.7\rho_{0,crit} &&\Longrightarrow \Omega_{0,\Lambda} \simeq 0.7. \end{aligned} \tag{1.1.13}$$

The Universe is therefore divided into eras of different component dominance. Given that the expansion parameter is related to the redshift z by

$$1 + z = \frac{a_0}{a},$$

we can compute the values of z corresponding to transitions between these eras. Matter-radiation equivalence occurs when

$$\begin{aligned}\rho_{0,M}\left(\frac{a_0}{a}\right)^3=\rho_{0,R}\left(\frac{a_0}{a}\right)^4 &\implies \rho_{0,M}(1+z_{eq})^3=\rho_{0,R}(1+z_{eq})^4\\ &\implies 1+z_{eq}=\frac{\rho_{0,M}}{\rho_{0,R}}\simeq 10^4\\ &\implies z_{eq}\simeq 10^4\end{aligned}$$

For the equivalence between matter and Λ we obtain

$$\begin{aligned}\rho_{0,M}\left(\frac{a_0}{a}\right)^3=\rho_{0,\Lambda}\left(\frac{a_0}{a}\right)^0 &\implies \rho_{0,M}(1+z_{eq,\Lambda})^3=\rho_{0,\Lambda}\\ &\implies 1+z_{eq,\Lambda}=\left(\frac{\rho_{0,\Lambda}}{\rho_{0,M}}\right)^{1/3}\simeq 1.3\\ &\implies z_{eq,\Lambda}\simeq 0.3\end{aligned} \tag{1.1.14}$$

Flat Models

In the case of a flat Universe, $\Omega=1$ and (1.1.8) becomes

$$\left(\frac{\dot a}{a_0}\right)^2=H_0^2\left[\Omega_0\left(\frac{a_0}{a}\right)^{1+3w}+(1-\Omega_0)\right]=H_0^2\left(\frac{a_0}{a}\right)^{1+3w}=H_0^2(1+z)^{1+3w}.$$

We can obtain the evolution of the scale factor

$$a(t)=a_0\left(\frac{t}{t_0}\right)^{\frac{2}{3(1+w)}},$$

which means infinite expansion.

Interestingly, the term $(1-\Omega_0)$ of (1.1.8) becomes negligible with respect to the other terms of the parentheses if

$$\left(\frac{a_0}{a}\right)^{1+3w}\gg\frac{|1-\Omega_0|}{\Omega_0}\implies\left(\frac{a_0}{a}\right)=1+z\gg\left(\frac{a_0}{a*}\right)=1+z*,$$

with

$$a*=a_0\left(\frac{\Omega_0}{1-\Omega_0}\right)^{\frac{1}{1+3w}}. \tag{1.1.15}$$

As a consequence, at early times all models behave as if $\Omega=1$, namely curvature can be ignored when studying models close to Big Bang.

Closed Models

Let's consider $\Omega_0>1$: we can find a time t_M so that the derivative $\dot a$ is zero. From (1.1.8), $\dot a=0$ if

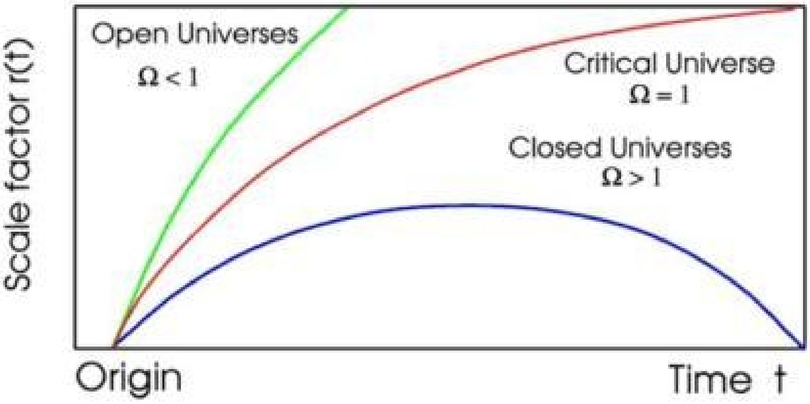

Figure 1.1: Evolution of the expansion parameter $a(t)$ for a flat Universe ($\Omega_0 = 1$ in red), for an open Universe ($\Omega_0 < 1$ in green), and for a closed Universe ($\Omega_0 > 1$ in blue). Image from Ian Morison [16].

$$1 - \Omega_0 = \Omega_0 \left(\frac{a_0}{a}\right)^{1+3w} \implies a_M = a_0 \left(\frac{\Omega_0}{1-\Omega_0}\right)^{\frac{1}{1+3w}}. \tag{1.1.16}$$

t_M corresponds to a maximum of the function $a(t)$, and after this time it starts to decrease until reaching zero at $t = 2t_M$.

Open Models

If $\Omega_0 < 1$, the term inside the square brackets of (1.1.8) is always positive, and for $a(t) \gg a(t*) = a*$ (see 1.1.15), the first term becomes close to zero and we can write

$$\begin{aligned}\frac{\dot{a}^2}{a_0^2} = H_0^2 \left[(1-\Omega_0) + \Omega_0 \left(\frac{a_0}{a}\right)^{1+3w}\right] \simeq H_0(1-\Omega_0) &\implies \frac{\mathrm{d}a}{\mathrm{d}t} = \dot{a} = a_0 H_0 \sqrt{1-\Omega_0} \\ &\implies a(t) = a_0 H_0 \sqrt{1-\Omega_0}\,t \\ &\implies a(t) \propto t.\end{aligned}$$

Figure 1.1 shows the three fates of different models according to the value of the density parameter.

Models with Cosmological Constant

Friedmann equations for models with Λ are

$$\ddot{a} = -\frac{4\pi}{3}G\left(\rho + \frac{3p}{c^2} - 2\rho_\Lambda\right)a \tag{1.1.17}$$

$$\dot{a}^2 + kc^2 = \frac{8\pi}{3}G(\rho + \rho_\Lambda)a^2, \tag{1.1.18}$$

where

$$\rho_\Lambda = -\frac{p_\Lambda}{c^2} \equiv \frac{\Lambda c^2}{8\pi G}. \tag{1.1.19}$$

In recent years, cosmological data from experiments with great accuracy (Cosmic Microwave Background measurements, Ia Supernovae, Baryon Acoustic Oscillations surveys) have shown that today the Universe is accelerating while expanding, a behaviour that cannot arise from any of the models treated in the previous sections. The expression 'Dark Energy' indicates a form of unknown energy as the possible mechanism responsible for the accelerating expansion of the Universe.

In (1.1.3) we have demonstrated that a negative pressure would lead to a repulsive gravitation, and an accelerating expansion means that $\ddot{a} > 0$, but it can be easily shown that models made of fluids with $-1/3 < w$ have the property

$$\ddot{a} = -\frac{4\pi}{3}G\left(\rho + \frac{3p}{c^2}\right)a = -\frac{4\pi}{3}Ga\rho(1+w) < 0.$$

Therefore, there must exist a point in time where $\ddot{a} = 0$, in other words an inflexion point (**Figure 1.2**).

The cosmological constant is the simplest form of Dark Energy because it requires the least number of degrees of freedom (i.e. zero: only a constant) and features a non-varying density as the Universe expands, and this leads to the current model of cosmology being called ΛCDM and often referred to as *standard cosmological model.*

1.2 On Structure Formation

According to the Cosmological Principle, the Universe is homogeneous and isotropic at sufficiently large scales; however, observational data reveal a richness of detail on scales from galaxies to large-scale structures (up to 100 Mpc). The evidence of these structures allows us to learn something about the initial conditions of the Universe and the processes under which these evolved.

The central point of studying cosmological inhomogeneities is to understand how the Universe departed from uniform density. If we imagine a fluid made of both matter and radiation, the simplest way to change its density is by contraction and expansion, which can be accomplished by adiabatic perturbations of density.

These are thought to be the resulting fluctuations created at the final stages of inflation, a process that occurred in the early Universe characterized by a very fast expansion which made quantum fluctuations to grow to macroscopic scales.

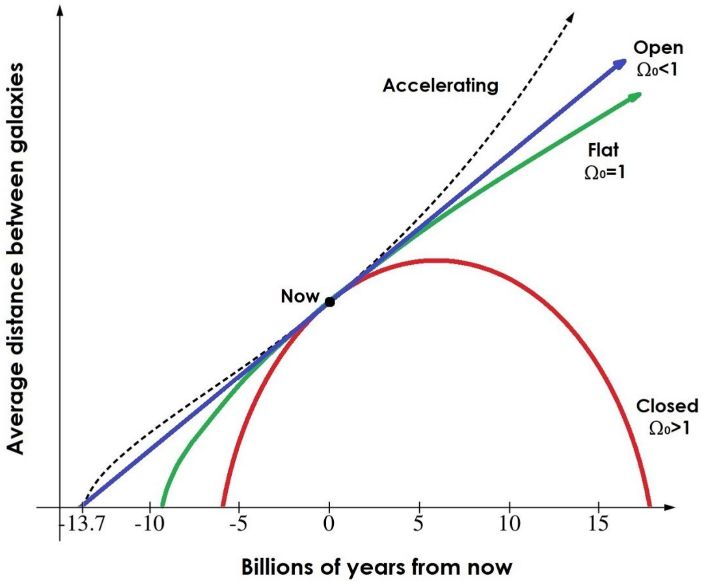

Figure 1.2: Evolution of the expansion parameter $a(t)$ for different models. Note as at present time being able to identify the right parametrization of the Big Bang model is not trivial. Image from Helen Klus [12].

Jeans demonstrated that small fluctuations can increase under some conditions; his theory, developed in an epoch when the Universe was thought to be static, can be applied without further modifications to star and planet formation, as they form in a quite static background.

A qualitative approach is to consider two processes: gravitational force which tends to attract particles, and gas pressure which acts in the opposite direction. If the effect of pressure is much smaller than the tendency of self-gravity of a density fluctuation to induce collapse, an overdense region can start to accrete material, becoming denser and denser until an instability is formed, which will eventually cause the collapse of the fluctuation to a gravitationally bound structure. Equilibrium occurs when

$$F_p + F_g = 0 \implies \frac{GM}{R^2} = p\frac{R^2}{M} = \frac{c_s^2}{R} \implies R_J = \frac{c_s^2}{\sqrt{G\rho}}$$

where we have substituted p with ρc_s. R_J is called the *Jean's scale* and if $R > R_J$, gravitation overcomes pressure.

1.2.1 Jeans Theory

One of the most important aspects in the study of fluid dynamics is the analysis of the conditions under which a perturbation can generate instabilities. These can develop as a consequence of small perturbations passing through the fluid, and the way they grow and evolve is the essence of *linear* and *nonlinear* theory.

In Newtonian approximation, the most generic equations governing motion of fluid are

$$\begin{aligned} &\frac{\partial \rho}{\partial t} + \nabla \cdot \rho \mathbf{u} = 0 && \text{Continuity equation} \\ &\frac{\partial \mathbf{u}}{\partial t} + (\mathbf{u} \cdot \nabla)\mathbf{u} + \frac{1}{\rho}\nabla p + \nabla \phi = 0 && \text{Euler equation} \\ &\nabla^2 \phi - 4\pi G \rho = 0 && \text{Poisson equation} \end{aligned}$$

Let's now consider a homogeneous medium at constant density, pressure, and gravitational field (ρ_0, p_0, ϕ_0), initially at rest ($\mathbf{u}_0 = 0$). Infinitesimal perturbations will modify these quantities for a generic fluid element such that

$$\begin{aligned} p &= p_0 + \delta p \\ \rho &= \rho_0 + \delta \rho \\ \mathbf{u} &= \delta \mathbf{u} \\ \phi &= \phi_0 + \delta \phi. \end{aligned}$$

And the equations become (neglecting second order terms)

$$\begin{aligned} &\frac{\partial \delta \rho}{\partial t} + \rho_0 \nabla \cdot \delta \mathbf{u} = 0 \\ &\frac{\partial \delta \mathbf{u}}{\partial t} = -\frac{1}{\rho_0}\nabla \delta p - \nabla \delta \phi \\ &\nabla^2 \delta \phi = 4\pi G \delta \rho. \end{aligned}$$

Taking δp as $c_s^2 \delta \rho$, the time derivative of the first equation, and the divergence of the second, we can express $\nabla \delta \phi$ by means of the third equation to obtain

$$\begin{aligned} &\frac{\partial^2 \delta \rho}{\partial t^2} + \rho_0 \nabla \cdot \frac{\delta \mathbf{u}}{t} = 0 \\ &\rho_0 \nabla \cdot \frac{\partial \delta \mathbf{u}}{\partial t} = -c_s^2 \nabla^2 \delta \rho - 4\pi G \rho_0 \delta \rho \end{aligned} \implies \frac{\partial^2 \delta \rho}{\partial t^2} = c_s^2 \nabla^2 \delta \rho + 4\pi G \rho_0 \delta \rho. \quad (1.2.1)$$

Jeans imposed the solutions to be in the form of plane waves

$$f(r,t) = f_k \exp\left[\mathrm{i}\,\mathbf{k} \cdot \mathbf{r} + i\omega t\right],$$

where f_k is the amplitude, $\mathbf{k}$ is a wavevector, $\mathbf{r}$ is a position vector, and ω is a frequency which is in general complex.

Thereby, (1.2.1) becomes the following dispersion relation

$$w^2 = k^2 c_s^2 - 4\pi G \rho_0,$$

after imposing

$$\delta \rho = \delta \rho_k \, \mathrm{e}^{\mathrm{i}\,\mathbf{k} \cdot \mathbf{r} + \mathrm{i}\,\omega t}.$$

Instability arises when w is imaginary, namely when $k^2 c_s^2 - 4\pi G \rho_0 < 0$.

Therefore, the solutions are of two kinds, depending on whether the wave length $\lambda = 2\pi/k$ is greater or smaller than

$$\lambda_J := \sqrt{\frac{\pi c_s^2}{G\rho}}.$$

λ_J is known as *Jeans length* and the criterion for gravitational instability states that structures larger than λ_J within a medium should feel their own self gravity and collapse.

The density content can be divided into radiation and nonrelativistic matter, each having a distinct perturbation mode, with different relations between the two density components. However, we should keep in mind that these components are not completely independent as they feel the same gravitational potential.

1.2.2 Jeans Theory: expanding Universe

In studying structure formation in expanding universes things get more complicated, as matter density varies with time. We also have to take into account the different behaviour of relativistic and nonrelativistic fluids, along with the matter component dominance in a certain epoch. Basically we have to translate Jeans Theory into the language of the Friedmann models, which could be non trivial, so it is better to divide cases.

Outside the cosmological horizon structures are not connected, and in this respect, only gravity matters. Let's consider perturbations to be a little spheric Universe ($\Omega > 1$), overdense with respect to a background, flat Universe ($\Omega = 1$). The second Friedmann equation takes the forms

$$\begin{aligned} H_p^2 + \frac{c^2}{a^2} &= \frac{8\pi}{3} G\rho_p \\ H_b^2 &= \frac{8\pi}{3} G\rho_b, \end{aligned}$$

where the subscripts p and b indicate perturbation and background quantities, respectively. We now impose that the equations have the same H:

$$\frac{8\pi}{3} G\rho_p - \frac{c^2}{a^2} = \frac{8\pi}{3} G\rho_b \implies \rho_p - \rho_b = \frac{c^2}{a^2} \frac{3}{8\pi G}. \tag{1.2.2}$$

We can apply the definition of density contrast

$$\delta := \frac{\delta\rho}{\rho} = \frac{\rho_p - \rho_b}{\rho_b}$$

so that equation 1.2.2 becomes

$$\frac{8\pi}{3} G\rho_b \delta = \frac{c^2}{a^2} \implies \delta \propto \frac{1}{a^2 \rho_b}.$$

We have seen in 1.1.11 that

$$\rho \propto a^{-3(1+w)},$$

and w varies according to whether Universe is before of after equivalence:

$$\begin{aligned} t < \quad & t_{eq} \implies w = \frac{1}{3} && \implies \delta_R && := \delta \propto a^2 \\ t > \quad & t_{eq} \implies w = 0 && \implies \delta_M && := \delta \propto a \end{aligned}$$

Inside the cosmological horizon, one should retake the calculus for a static Universe (namely the Jeans approach seen before) considering this time comoving coordinates as well, related to the physical coordinates by

$$\mathbf{r} = \mathbf{r}_0 \frac{a}{a_0}.$$

Now the solutions we are looking for are in form of plane waves with amplitude depending on time due to the expansion. The resulting perturbation equations are

$$\dot{\delta}_k + \mathrm{i}\,\mathbf{k}\frac{v_k}{a} = 0 \tag{1.2.3}$$

$$\dot{\mathbf{v}}_k + \frac{\dot{a}}{a}\mathbf{v}_k = \frac{\mathrm{i}\,\mathbf{k}}{a}\left(c_s^2\delta_k + \delta\phi_k\right) \tag{1.2.4}$$

$$\delta\phi_k = -\frac{4\pi G\rho_b\delta_k a^2}{k^2} \tag{1.2.5}$$

We can simplify the first equation by considering the two components of velocity. Since δ_k and $\delta\phi_k$ are parallel to $\mathbf{k}$, vertical solutions can be obtained from (1.2.4)

$$\dot{\mathbf{v}} + \frac{\dot{a}}{a}\mathbf{v} = 0 \implies \mathbf{v} = \mathbf{v_0}\frac{a_0}{a}.$$

This component is destined to become fainter and fainter as the Universe grows and expands, so we can keep the horizontal part of the velocity field.

From the derivative of (1.2.4) we obtain the dispersion relation

$$\ddot{\delta}_k + 2\frac{\dot{a}}{a}\dot{\delta}_k + \left(k^2c_s^2 - 4\pi G\rho_b\right)\delta_k = 0. \tag{1.2.6}$$

Solutions of the equation describe the growth of perturbations and hinge on the cosmological background model.

In the case of a flat, matter-dominated Universe solutions are in the form of a power law and can lead either to an increasing or a decreasing perturbations growth

$$\delta_k \propto t^\alpha \implies \begin{array}{lll} \delta_- & \propto t^{-1} & \propto a^{-3/2} \\ \delta_+ & \propto t^{2/3} & \propto a \end{array}$$

where the increasing δ_+ solution is the one we are interested in, and since expansion acts against the growth, in this model the evolution of fluctuations is slower than the static model (where the increase was in the form of exponential), as expected.

For curved models there is not an analytical solution, instead the analysis is carried by means of numerical simulations on the dispersion relation

$$\delta_+(z) = -\frac{H(z)}{a_0^2}\int\frac{1+z}{H^3(z)}dz.$$

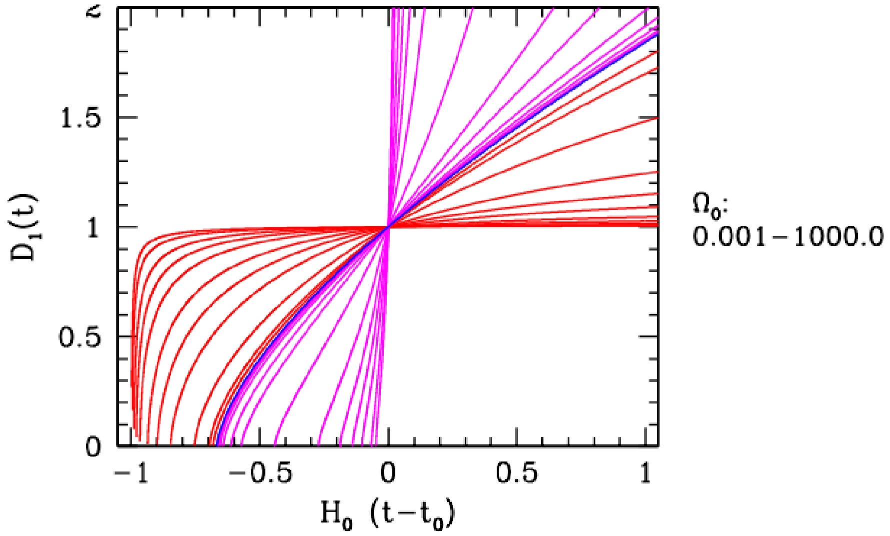

Figure 1.3: Linear density growth factor δ_+ from different FRW universes as a function of cosmic time. Blue: flat universes, red: open universes, pink: closed universes. Image from Rien van de Weijgaert [27].

Figure 1.3 shows the evolution of density fluctuations δ_+ for flat, closed, and open matter-dominated universes inside the cosmological horizon.

In the limit case of $\Omega_0 = 0.001$ perturbations cannot grow at all, while for highly overdense universes they grow faster than for the flat model.

Looking back in time from now we can build the history of fluctuations, i.e. by analysing the slope of the three curves starting from the present time we can make predictions about how many structures could have formed according to the cosmological model. For instance, one expects to find a larger number of objects at $z = 1$ in an open Universe than in a closed one, because in the latter case perturbations grow faster so they have to start their growth later. This kind of study is made with cluster counts.

Another way to measure today's amplitude of fluctuations with respect to the predictions of models is by the analysis of the Cosmic Microwave Background, which is the oldest electromagnetic radiation in the Universe and permeates all the space. CMB indicates the point in time where radiation and baryons decoupled, due to the creation of hydrogen atoms which have a far smaller cross section than electrons, so that the mean free paths of photons becomes infinite and they start to travel across the Universe.

Temperature anisotropies in the CMB spectrum allow us to compute the amplitude of perturbations at the redshift of decoupling, and observational probes account for a value of $\delta T/T \simeq 10^{-5}$ at $z_{dec} \simeq 1100$. We have seen that a flat Universe comprised by matter has a growth of fluctuations of $\delta_+ \propto t^{2/3} \propto a$, so that we can write

$$\delta_{t_0} = \delta_{t_{\rm CMB}} \delta_+ \simeq 10^{-5} 10^3 \simeq 10^{-2}.$$

This is only a rough estimate though it allows us to measure the order of magnitude of the fluctuation amplitude we should see today; however, galaxies

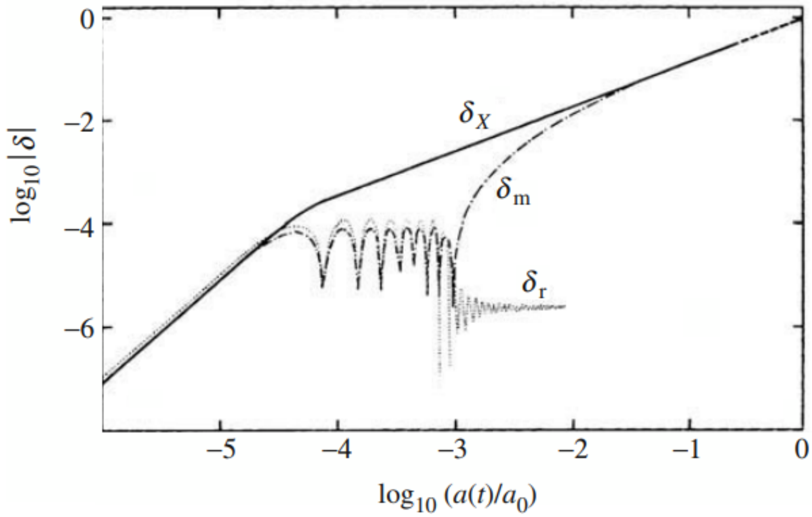

Figure 1.4: Evolution of $\log\delta$ for a Dark Matter dominated model, where the subscript X indicates DM, m represents the baryonic component, and r is for radiation. After decoupling, baryons experience a faster growth, while radiation continues to oscillate. Image from Frank van den Bosch [28].

and clusters provide values four-five orders of magnitude larger than that.

A difference as such cannot be due to baryonic matter alone, since the growth factor is too small and would cause a 10^{-2} amplitude of fluctuation, but it is generated by the effect of Dark Matter, which decouples earlier from radiation than baryons, and then creates deeper and earlier potential wells that would guide the gravitational collapse.

When baryons decouple from radiation, fluctuations in their density distribution can start to increase following the guidance of dark matter potential wells and that means at the time of decoupling the Universe was already inhomogeneous. The presence of overdense regions eases the development of density perturbations, causing a process known as **baryon catch up**. A fast growth as such allows even tiny density fluctuations of baryons to reach the size we observe today (**Figure 1.4**).

The equation governing the evolution of baryon density perturbations is

$$\delta_{k,b} = \delta_{\mathrm{DM}}\left(1 - \frac{a_{dec}}{a}\right).$$

When $a \gg a_{dec}$, the amplitude of baryons and DM fluctuations is the same.

1.2.3 Cosmological Perturbations

Jeans Theory is based on the assumption that linear perturbations can be described as superposition of plane waves which evolve independently, so that the final result is expected to be a structure generated by the growth of fluctuations on different scales.

The spectral composition is derived in the Fourier space, where the density contrast takes the form

$$\delta(\mathbf{x}) = \sum_k \delta_{\mathbf{k}} \exp\left(\mathrm{i}\,\mathbf{k}\cdot\mathbf{x}\right),$$

where $\mathbf{x}$ is the position vector, and each $\delta_{\mathbf{k}}$ is different from another for amplitude and phase. If the latter is random, then the density field has Gaussian statistics. Variance can be calculated as the expectation value computed over a number of realizations of the Universe and results to be

$$\sigma^2 \equiv \left\langle \delta^2 \right\rangle = \sum_k \left\langle |\delta_{\mathbf{k}}|^2 \right\rangle = \frac{1}{V}\sum_k \delta_k^2,$$

where V is the volume of a statistically fair sample of the Universe. Taking the limit of a very large V, and assuming the density field being homogeneous and isotropic we can write

$$\sigma^2 = \frac{1}{2\pi}\int_0^\infty P(k)k^2\,\mathrm{d}k.$$

$P(k)$ is called the **power spectrum** and it is proportional to $\left\langle \delta_k^2 \right\rangle$.

Variance depends only on time, so that it can give information about the perturbation amplitudes but does not provide insights on their spatial structure.

The analogous quantity in real space is called the *two-point correlation function* and it is expressed by

$$\xi(\mathbf{r}) = \xi(r) = \xi\left(|\mathbf{x}_1 - \mathbf{x}_2|\right) = \left\langle \delta(\mathbf{x}_1)\delta(\mathbf{x}_2) \right\rangle.$$

It is linked to the power spectrum by the Fourier transform.

1.2.4 Nonlinear Regime

In order to gain a full description of structure formation nonlinear regime is needed, since Jeans process works perfectly fine as long as $\delta \ll 1$. However, overdensities can reach considerably higher values, and when dark matter halos begin to form they are far over unity. For instance, a galaxy cluster has typical overdensities of 10^{2-3}. For this reason it is critical to understand the processes that modify the simple linear evolution growth laws in these cases.

The simplest approach to nonlinear theory leads to a **spherical collapse** and it does have a great cosmological relevance despite not being sufficient since it considers spherical perturbations with constant density, while they are supposed to be random and with an irregular shape.

The key-point of the analysis is to consider the overdense region like a mini Universe, for which the evolution has been already seen. An overdense Universe is destined to collapse after reaching the maximum of expansion in a time $2t_M$ (1.1.16).

Conversely, in this case collapse stops when virial equilibrium is reached. If we take the virial equation

$$E_k = -\frac{1}{2}E_p,$$

at $t = t_M$ the sphere ceases to expand, so that all energy is in the form of potential energy

$$E_p = -\frac{3GM^2}{5r_{\rm max}}.$$

Let's consider the time at which the spherical region has collapsed by a factor 2 from its maximum expansion, namely $r = r_{\rm max}/2$ and

$$E_p = -\frac{3GM^2}{5r_{\rm max}/2} = -\frac{6GM^2}{5r_{\rm max}}.$$

From the equation of energy conservation

$$E_k = E - E_p = -\frac{3GM^2}{5r_{\rm max}} + \frac{6GM^2}{5r_{\rm max}} = -\frac{1}{2}E_p\left(\frac{r_{\rm max}}{2}\right),$$

which is the condition for equilibrium according to the virial theorem. As a consequence, one can calculate an estimate for the density contrast expected at the end of this process, as the ratio between the density in the perturbation and the mean density of the Universe

$$\rho_p(t_{\rm vir}) = 180\rho_b(t_{\rm vir}).$$

Once a nonlinear object is born, it continues to accrete matter from the surroundings. Therefore, it is interesting to investigate what happens at later times, when the collapse has gone completely nonlinear.

The complexity of the processes involved in this regime makes it impossible to reach analytical solutions, thus numerical simulations step in. They are based on numerical integration of the equations of motion for a very large number of particles that are given small initial perturbations, and in general they have to take into account all processes related to structure formation, like halo merging, gas cooling, star formation, stellar spectral and chemical evolution, and AGN feedback. For large scale structures we should though remember that most of them yield only a mild effect.

Cosmological simulations exploit initial conditions for the density fluctuations compatible with the result of the CMB, and then they evolve these perturbations until present day. Different models lead to different results in structure formation which are in turns compared to observational data.

Chapter 2

Non-standard Cosmologies

2.1 ΛCDM: a not-so perfect model

Modern cosmology can be seen as a giant box of extremely precise data with the problem to find a suitable model to describe them all. How is it possible to choose between the large amount of existing parametrizations? The quest for the perfect model is based on criteria of simplicity and naturalness, which had led to the present ΛCDM.

The standard cosmological model is characterized by a dominant component with a constant equation of state $w = -1$, and a Cold Dark Matter component in the form of weakly interacting particles having a very low velocity dispersion called WIMPs (Weakly Interacting Massive Particles).

While there is an intense effort towards a direct detection of DM, today we do not have any proposed laboratory experiments to investigate the physics related to Λ.

ΛCDM turned out to be successful as a model, since its predictive power being tested in recent precisely observational discoveries (e.g. lensing of the Cosmic Microwave Background [24] and the kinetic Sunyaev-Zel'dovich effect [9]). However, it suffers from both observational and theoretical drawbacks.

From an observational point of view, tensions seem to come from recent observational data at low z such as cluster counts [7], redshift space distortions [22], weak lensing data [11], and local measurements of the Hubble constant H_0 [21], which point towards a lower rate of structure growth (a lower σ_s) than the Planck results based on ΛCDM predictions.

On the other hand, theoretical issues arise with respect to the fundamental properties of DE seen in the previous chapter. In particular, there are two unresolved problems, namely the *fine tuning* and *coincidence* problems.

2.1.1 The Fine Tuning Problem

The fine-tuning problem associated with the cosmological constant is part of a bigger set of conditions which comprise the Fine-tuned Universe topic. This is a proposition stating that all present variables are confined into a considerable narrow range of values in order to allow life to occur [10].

As regards to Λ, the problem arises when measuring the value of the cosmological constant.

We have seen that

$$\rho_\Lambda = -\frac{p_\Lambda}{c^2} = \frac{\Lambda c^2}{8\pi G}. \tag{1.1.17}$$

and since recent measurements give $\Omega_\Lambda = 0.68$ and $\rho_{0,crit} = 1.9{\cdot}10^{-29}h^2$ g/cm^3, from

$$\Omega_\Lambda = \frac{\rho_\Lambda}{\rho_{0,crit}},$$

we can derive the value of Λ, which turns out to be

$$\rho_\Lambda = -\frac{p_\Lambda}{c^2} = \frac{\Lambda c^2}{8\pi G} \implies \Lambda = \frac{8\pi G\rho_\Lambda}{c^2} \simeq 10^{-56} \quad \mathrm{cm}^{-2}$$

This value is surprisingly low, considering the importance of Λ in determining the fate of our Universe, however if Λ were higher it would prevent structures to form, and from this consideration the fine-tuning problem is born.

2.1.2 The Coincidence Problem

We have seen in Chapter I that the densities of the Universe constituents evolve differently and so the cosmic history can be divided into eras of dominance. According to the Big Bang model, at early times radiation was the most important component, and short after ($z_{eq} \simeq 10^3$) the equivalence between radiation and matter occurs, as the Universe expands while cooling. z_{eq} represents the beginning of the matter-dominated epoch, in which structures can form. This status is theoretically meant to last forever, except for the rise of a third epoch characterised by the DE dominance.

The DE phase started when (dark) matter had reached the same density of DE, which has been computed in (1.1.12) to be quite near to the present time. Since then the Universe experienced a growth in its rate of expansion and gravity became unable to generate nonlinear collapsed structures.

Given the still unknown nature of the dark sector, it is remarkable that dark energy and dark matter possess the same order of magnitude of density today, like we are living in a special time. This fact appears to be a coincidence because it requires very fine-tuned initial conditions in the primordial Universe.

A great number of DE models has been proposed in order to give an explanation to the Cosmological Coincidence Problem (CCP), and in general solutions invoke a nonstandard behaviour of the DE fluid at different epoch or interaction models. Other theories involve the so-called anthropic principle, so that some scientists do not see the CCP as a problem, arguing that we are indeed living in a special period which is unique.

One can see that the fine-tuning problem and the coincidence problem are distinct for models featuring a variable equation of state, while in the case of cosmological constant they can be considered as the same problem.

2.2 Dark Energy Models

Theorical problems related to the cosmological constant seem to arise from its nonevolving nature, thus the research for alternative models with dynamically evolving scalar field is strongly fostered.

Quintessence was first presented as a viable cosmological scenario by Ratra and Peebles (1988) [20], and its basic concept was later extended to a variety of evolving dark energy models [5]. The energy density and pressure of this scalar field are in the form

$$\rho_Q = \frac{1}{2}\dot{\phi}^2 + V(\phi) \tag{2.2.1}$$

$$p_Q = \frac{1}{2}\dot{\phi}^2 - V(\phi), \tag{2.2.2}$$

where $\frac{1}{2}\dot{\phi}^2$ is the kinetic energy and $V(\phi)$ is the potential energy. $V(\phi)$ determines the evolution of the density and thus the expansion history and the formation of structures; it can takes different forms such as th exponential law [29] and the inverse power-law [20]

$$V(\phi) = V_0 e^{\frac{-\lambda\phi}{M_{\rm PI}}} \tag{2.2.3}$$

$$V(\phi) = V_0 e^{\frac{-\lambda}{M_{\rm PI}}}, \tag{2.2.4}$$

where $M_{\rm PI}$ is the reduced Plack mass given by $M_{\rm PI} \equiv 1/\sqrt{8\pi G}$.

From (2.2.1) and (2.2.2) we can write the expression of the equation of state

$$w_Q = \frac{p_Q}{\rho_Q} = \frac{\frac{1}{2}\dot{\phi}^2 - V(\phi)}{\frac{1}{2}\dot{\phi}^2 + V(\phi)}. \tag{2.2.5}$$

w_Q ranges between -1 and 1: the scalar field behaves like a cosmological constant if w_Q is closed to -1, namely if ϕ evolves slowly, resulting in the kinetic term being considerably smaller than the potential energy term.

Given that the precise nature of the two dark sectors is at present unknown, there remains ample scope for either DM and DE to be described by a fundamentally new kind of physics.

It has been demonstrated [8] that there are quintessence models (such as the ones characterized by a potential energy in the form of 2.2.3 or 2.2.4) capable of providing a partial solution for the cosmological constant problems, as they feature a density which *tracks* the radiation density until the equivalence time and then it starts to become similar to Λ.

Another possibility is to assume a parametrization of the equation of state parameter, so that it varies with redshift (the scalar factor). In this project thesis we have considered two of these parametrizations, namely the Chevallier-Polarski-Linder (CPL hereafter, [6,14]) and a hyperbolic tangent function (HYP hereafter, [4]). The former has an equation of state parameter given by

$$w_{\rm CPL}(a) = w_0 + (1-a)w_a, \tag{2.2.6}$$

$w_{\rm CPL}$ ranges between w_0 for $z = 0$ and $(w_0 + w_a)$ for $z \to \infty$, with a negative convexity. w_a represents the low-redshift evolution of $w_{\rm CPL}$.

The HYP parametrization is characterized by

$$w_{\rm HYP}(a) = w_0 + \frac{w_a}{2}\tanh\left(\frac{1}{a} - z_t\right). \tag{2.2.7}$$

$w_{\rm HYP}(a)$ has the same interval range of value of $w_{\rm CPL}$, while its evolution is different (see **Figure 2.1**).

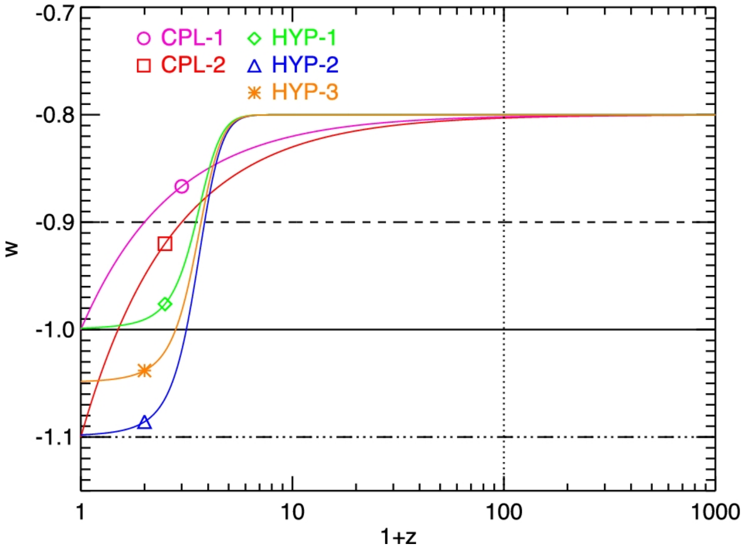

Figure 2.1: The evolution of w for different models. The two variable-w parametrisations of our interest are HYP-1 (green line) and CPL-2 (in red). Image from Baldi and Simpson [4].

2.3 Dark Scattering Models

Since the precise nature of the two constituents of the dark sector is still unknown, there is an ample variety of models in the literature which invoke a new form of physics for the description of either DM and DE.

Generally speaking, an interaction between dark energy and dark matter could lead to different results, namely there may be an exchange of energy, a momentum transfer, or the formation of new particles. We know that elastic scattering usually occurs when non-relativistic particles collide, while inelastic scattering is more likely to happen in relativistic impacts which do not conserve the energy of the incident particles. The choice of elastic interaction seems therefore more desirable given the extremely low dark energy density and the non-relativistic velocities related to the dark matter motions.

Dark Scattering Models were first proposed as an alternative theory to the ΛCDM standard model in 2010 [23]. They comprise a class of models characterized by elastic scattering between DE and DM.

The scattering cross-section σ can be regarded as the likelihood of a scattering event since it represents the target area seen by an incident particle. For these models, the scattering cross-section between DE and DM σ_D gains a nonzero value.

We have seen in Chapter 1 that the formation of structure is based on gravitational instability, which stems from the growth of small primordial perturbations. In linear theory, density and velocity perturbations δ and θ evolve according to a system of differential equations which has been extensively studied in a number of papers (see e.g. [15]), and then modified for dark scattering models in [3, 4, 23]. In particular, the velocity perturbations become

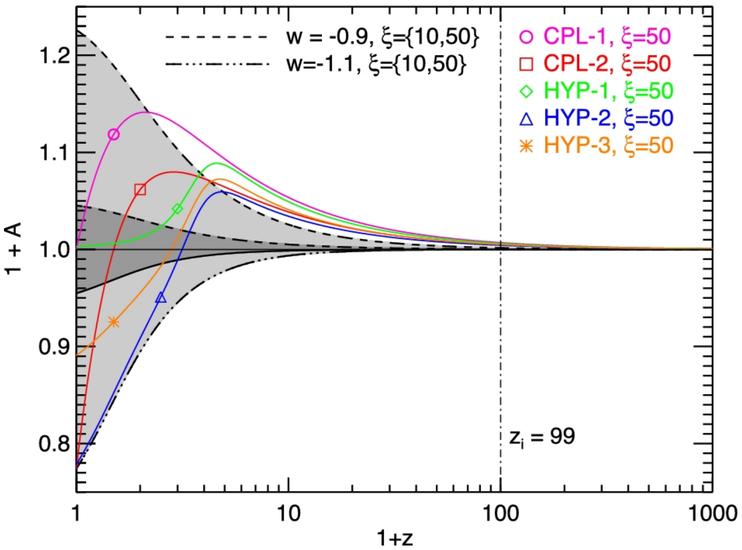

Figure 2.2: The evolution of A as a function of w for different models. The two variable-w parametrisations of our interest are HYP-1 (green line) and CPL-2 (in red). Image from Baldi and Simpson [4].

$$\theta'_{\mathrm{DE}} = 2H\theta_{\mathrm{DE}} - an_D\sigma_D\Delta\theta + k^2\phi + k^2\frac{\delta_{\mathrm{DE}}}{1+w} \tag{2.3.1}$$

$$\theta'_{\mathrm{CDM}} = -2H\theta_{\mathrm{CDM}} + \frac{\rho_{\mathrm{CDM}}}{\rho_{\mathrm{CDM}}}(1+w)an_D\sigma_D\Delta\theta + k^2\phi, \tag{2.3.2}$$

where n_D is the proper number density contrast, $\Delta\theta = \theta_{\mathrm{DE}} - \theta_{\mathrm{CDM}}$ is the velocity contrast, and the sound speed is taken $c_s^2 = 1$. The last assumption makes the DE density and velocity fields being homogeneous, so that their perturbations are expected to be near to zero and $\Delta\theta \simeq -\theta_{\mathrm{CDM}}$. This was also demonstrated in [3]. We can now rewrite (2.3.2) to point out the friction term A dependence

$$\theta'_{\mathrm{CDM}} = -H\theta_{\mathrm{CDM}}[1+A] + k^2\phi,$$

where

$$A := \frac{\rho_{\mathrm{DE}}}{H\rho_{\mathrm{CDM}}}(1+w)n_{\mathrm{CDM}}\sigma_D = (1+w)\frac{\sigma_D}{m_{\mathrm{CDM}}}\frac{3\Omega_{\mathrm{DE}}}{8\pi G}H. \tag{2.3.3}$$

A can either assume positive and negative values, namely it can act both as a friction and a drag force, according to w. In fact, A will be positive or negative for $w > -1$ or $w < -1$, and its evolution in time as a function of w is showed in **Figure 2.2**.

The central point of this work is to study how the presence of an additional drag/friction term impacts on the growth of structures. We considered 5 cosmological models: the reference ΛCDM model, two dark scattering models with a time-dependent DE equation of state parameter w_{CPL} and w_{HYP} (see 2.2.6 and

2.2.7), and two dark scattering models characterized by a constant DE equation of state parameter $w = -1.1$ and $w = -0.9$.

Baldi and Simpson [3, 4] carried out an analysis on these models, showing that a scattering between DE and DM may provide a suppression of structure formation which could alleviate the tensions between observational data and ΛCDM predictions presented at the beginning of the chapter.

Their results provide useful insights into some basic properties of dark matter halos, such as the nonlinear power spectrum, the halo mass function, and the concentration-mass relation. They showed that $w = -1.1$ models provide an enhancement of the linear perturbation amplitude and a suppression in the nonlinear regime. The opposite effects has been detected for $w = -0.9$ models.

Here, we want to extend the analysis by studying the effects of these dark scattering models mainly on two observables: the density and velocity profiles of dark matter halos.

From a theoretical point of view, we expect two different effects of the friction term on a DM particle falling into a dark matter halo potential well. In linear regime, the particle possesses a radial direction of motion so that the friction term will act against it, causing the particle to slow down. When the particles enters in the nonlinear regime it starts to gain a tangential component of velocity and thus the friction term will enhance the loss of kinetic energy, making the infall happen faster. An opposite behaviour is expected for a drag term.

Therefore, velocity profiles are supposed to show smaller values for all dark scattering models characterized by a friction term at large scales (i.e. far from the centre of the halo), and a sort of catch-up in the inner regions, which is likely not to reach the ΛCDM curve. For models featuring a drag term higher values in velocities are expected.

Chapter 3

Cosmological Simulations

In Chapter 1 we discussed that an analytical approach cannot provide solutions to the evolution of perturbations in the nonlinear regime. Numerical simulations are a very powerful tool because they can allow us to follow the evolution of the most important processes in the Universe over the course of billion of years.

Simulations of large regions of the observable Universe have reached the remarkable order of magnitude of half a trillion particles [2], while zoom-in simulations of single halos are now performed with over a billion particles.

The range of scales these simulations can span is considerably large, from tens of parsec to 20 Gpc.

Over the last decade, many efforts were put in the development of more accurate algorithms and in the increase of the computational power, which have led to impressive progresses in a great number of fields of interest. For instance, the role of dark matter in the process of structure formation could be followed with great precision, thus resulting in the identification of the CDM paradigm as the scaffold for the formation of galaxies and galaxy clusters [13]. Moreover, at the present time simulations are broadly used to investigate the fundamental properties of dark energy as well, since they can provide a general overview on the main features of different DE models.

Depending on the type of analysis we want to conduct, we can make use of two approaches.

DM-only simulations take into account the sole effects of gravity, namely all matter is treated like collisionless dark matter. The basic idea is to consider a region of the Universe filled with a number N of DM particles which interact gravitationally, so that the analysis is carried out by means of N-body codes. N-body simulations are in general quite accurate given the plainer physics involved (see e.g. [26]).

We can distinguish between two kinds of these simulations, according to whether we are interested in exploring the large-scale structure of the Universe or focusing on a single halo. The former cover representative large volumes of the Universe (size between hundreds Mpc and tens Gpc) and thus play a crucial role in modelling the formation of DM halos. The latter aim to resolve the inner structure of a single halo and therefore require high resolution.

On the other hand, cosmological hydrodynamics simulations account for baryon physics and are based on the equations that govern a fluid motion (see Chapter 1).

3.1 N-body simulations

Pure dark matter simulations are simpler as the gravity is the only force involved; they are perfect for the analysis of density perturbation growth in non-linear regime, since DM decouples earlier from radiation with respect to baryon and for this reason at first only gravity acts on particles falling into the potential wells. The two fundamental equation governing gravity are the Euler equation and the Poisson equation, which can be written in their comoving form as

$$\frac{\mathrm{d}\mathbf{v}_i}{\mathrm{d}t} + 2\frac{\dot{a}}{a^2}\mathbf{v}_i = -\frac{1}{a^2}\nabla\phi = -\frac{G}{a^3}\sum_{i,j\neq i} M_j \frac{\mathbf{x}_i - \mathbf{x}_j}{|\mathbf{x}_i - \mathbf{x}_j|^3} = \frac{\mathbf{F}_i}{a} \tag{3.1.1}$$

$$\nabla^2\phi = 4\pi G\bar{\rho}(t)a^2\delta = \frac{3}{2}H_0^2\Omega_0\frac{\delta}{a}. \tag{3.1.2}$$

N-body codes try to solve this system of differential equations (we know that N-body problem cannot be solved analytically if $N \geq 3$) by taking N particles of mass M_i. The key-idea is to represent the density field as the sum of a set of test particles.

$$F_i = GM_i\sum_{i\neq j}\frac{M_j}{r_{ij}^2} \tag{3.1.3}$$

$$\frac{\mathrm{d}v_i}{\mathrm{d}t} = \frac{F_i}{M_i} \tag{3.1.4}$$

$$\frac{\mathrm{d}x_i}{\mathrm{d}t} = v_i. \tag{3.1.5}$$

The first equation defines the gravity as the force a particle experiences, the others define the acceleration and the velocity respectively.

All N-body codes work almost the same way as they make a time integration to derive acceleration and velocity once gravity is obtained

$$v_i(t+\Delta t) = v_i(t) + \frac{F_i}{M_i}\Delta t + \mathcal{O}(\Delta t^2) \tag{3.1.6}$$

$$x_i(t+\Delta t) = x_i(t) + v_i\Delta t + \mathcal{O}(\Delta t^2). \tag{3.1.7}$$

The main difference between codes is the way the force is computed. A first distinction can be made between procedures that obtain the force on the i-th particle directly from the Newton law, and the ones in which particles are put in grids and the force is calculated with Poisson law. The first are called Particle-Particle algorithms (PP), the latter are known as Particle-Mesh algorithms (PM).

3.1.1 Particle-Particle method

Here the force acting on the i-th particle is written as the sum on all particles of the system, as in (3.1.1)

$$F_i = \sum_{i,j\neq i} GM_j\frac{\mathbf{x}_i - \mathbf{x}_j}{|\mathbf{x}_i - \mathbf{x}_j|^3}. \tag{3.1.8}$$

This technique is simple yet it requires a considerably high number of operations because it takes into account every distance between particle pairs, therefore it is in general used for systems with $N < 10^6$ in which collisions play a major role. In fact, a perk of PP code is that it provides an exact law for the force.

Another drawback arises when the distance between two particles is very small, in particular one can see from (3.1.8) that the force diverges if particles' position coincides. One possible solution to this problem is to assume something like a finite size of particles which are otherwise treated as point masses.

3.1.2 Particle-Mesh method

The basic principle is that a set of particles is put into a grid of density values and the potential is computed for this density grid, then forces are applied to each particle according to the position of the cell in the grid and the position of the particle in the cell.

There are various ways to assign the density of particle in the grid. For example, one can take the *nearest grid point* so that a particle gives its mass to the closest point in the mesh. Another method is to distribute the mass to the points (typically 8 points for a 3D grid) surrounding the particle, with a weight based on distance (*Cloud-in-Cell*). This can be extended to the 9 surrounding boxes (*Triangular Shaped Cloud*).

Density of a grid point is given by

$$\rho(\mathbf{x}_{ijk}) = \sum_{i}^{N} w\left(\mathbf{x}_l - \mathbf{x}_{ijk}\right) \rho(\mathbf{x}_l).$$

with $w(\mathbf{x}) = w_i w_j w_k$ being the weight based on distance, and the subscript l indicated the particle's position. Once density is derived, gravitational potential is calculated in the Fourier space by resolving the Poisson equation which has the form

$$-k^2 \phi_k = 4\pi G \rho_k.$$

The gradient of the potential provides the force, which is transferred to the real space and then interpolated from the grid points.

PM algorithms are the fastest since they scale as $N \log N$, however the use of grids leads to a loss of resolution which is in part fixed by means of *Adaptive mesh* featuring adaptive grids. PM codes are therefore perfect for the analysis of very large set of particles (more than 10^9).

3.1.3 Partice-Particle/Particle-Mesh method

Since both PM and PP provide benefits and drawbacks, one can think of a combination of the two in order to create a more comprehensive procedure.

The basic idea is to use the PP on small scales and the PM on large scales: gravity is an additive force so that it can be divided in a short-range force computed directly (PP), and a long-distance force treated with the PM technique (*Partice-Particle/Particle-Mesh method*, P3M for short)

$$F_i = F_{\text{near}} + F_{\text{far}}.$$

One source of problems of this code is the definition of a critical distance that could allow us to link the two scales in order to have a clear transition from one to the other.

In the past decades PM and P3M algorithms were widely used for cosmological clustering studies, and the degree of clustering determined the choice between them. In dense environments the clustering is likely to be highly nonlinear so that it required the force resolution of P3M. On the other hand, for large-scale structures PM was generally preferred. Nowadays, P3M method has been overcome by the combination Tree-PM.

3.1.4 Tree codes

An alternative procedure is to build a *hierarchical tree* by a recursive division of the system into cells so that each of them comprises only a particle or none. Gravity is computed by direct sum (i.e PP) if particles are close, while if a group of particles is far from the i-th particle then all these particles are treated as a whole, and the mass is taken as the sum of all masses and stays at the mass centre of the set.

These codes need great memory resources and are quite complex to implement, however their high accuracy (no grids required) and velocity, along with a small calculus time ($\propto N \log N$) make them to be the best and most used algorithms at present day.

3.2 Hydrodynamic simulations

So far we have considered only DM since at the initial stages of structure formation gravity plays a major role and it drives DM particles to fall into the potential wells of the halos. After the decoupling with radiation, baryons are fastened in their collapse into the potential wells already formed, so that in the late stages of structure formation hydrodynamical effects become important.

Gas can be heated and cooled in various ways, and the physics involved is somewhat more complicated with respect to the N-body case, because there are different processes to take into account. While gravity acts on long distances, hydrodynamical events are effective only at small scales. The fundamental equations governing the motion of a fluid are the same presented in Chapter 1, with some extra terms representing the fenomena one wants to consider.

Whilst DM-only simulations works approssimately the same way and yield similar results, in the case of hydrodynamic simulations the choice of approach will lead to different outcomes. Basically there are two classes of methods: *Eulerian codes* use grids of points fixed in space and thus provide an accurate measurement of the evolution in time of the variables, while *Lagrangian codes* are characterised by a frame of reference moving with the fluid so that hydrodynamical quantities are computed in the particles' positions.

There are hybrid methods as well, which combine both Lagrangian and Eulerian approaches, and feature a grid of points to solve the fluid equations, which is deformable and follows the fluid in its motion.

3.3 Our simulation

In Chapter 2 we presented five cosmological models: ΛCDM, HYP, CPL, and the two wCDM models featuring $w = -0.9$ and $w = -1.1$. For all these scenarios, N-body simulations have been performed.

They are based on a modified version of the Tree-PM code GADGET (Springel [25]) which implements the drag force associated with the DE-CDM scattering.

For a generic particles' system moving into a fluid the acceleration is given by

$$\dot{\mathbf{v}}_{\mathbf{i}} = -\left[1 + A\right] H \mathbf{v}_i + \sum_{i \neq j} \frac{G m_j \mathbf{r}_{ij}}{|\mathbf{r}_{ij}|^3},$$

with (2.3.3)

$$A = (1 + w) \frac{3\Omega_{\mathrm{DE}}}{8\pi G} H\xi,$$

where ξ represents the strength of the interaction and it is given by

$$\xi \equiv \frac{c \cdot \sigma_D}{m_{\mathrm{CDM}}}.$$

In the range of models included in this project the choice for the scalar field self-interaction potential is the single exponential potential (2.2.3)

$$V(\phi) = V_0 e^{\frac{-\lambda\phi}{M_{\mathrm{Pl}}}},$$

which causes the scalar field to roll down the potential with positive velocity, reaching the normalization value $\phi = 0$ at the present time.

Initial conditions for N-body simulations are generated by displacing particles from a homogeneous distribution in order to set up a random-phase realization of the linear power matter spectrum of the cosmological model.

These particles are then rescaled to the desired amplitude of density perturbations at some z_i, which is taken equal to 99. As the same random seed for all the simulations is used, the resulting particle displacements are exactly the same for all the cosmological models at z_{eq} and the initial conditions for each individual run are then generated by rescaling forward the displacements amplitudes to $z_i = 99$ with the correct growth factor computed for each cosmological model. This way, all the different expansion history of the density perturbations in the various expanding universes that will come out can be unambiguously ascribed to the effects of different cosmological models.

The effective drag force is proportional to the combination $\Omega_{\mathrm{DE}} H$ which rapidly vanishes at high redshifts for our set of cosmologies.

The size of the box is 1 comoving Gpc/h a side, filled with 1024^3 CDM and baryon particles. The mass resolution is $m_c = 5.84 \cdot 10^{10}$ $\mathrm{M}_\odot/h$ for CDM particles and $m_b = 1.17 \cdot 10^{10}$ $\mathrm{M}_\odot/h$ for baryons.

Even if hydrodynamics is not included so that the simulations are purely collisionless N-body, the presence of baryons allows us to compute a more realistic scenario, since without them the effect of coupling would be overestimated. In fact, CDM and baryons do not follow the same dynamics, as baryons are uncoupled to the dark sector and we can assume they obey Newtonian laws,

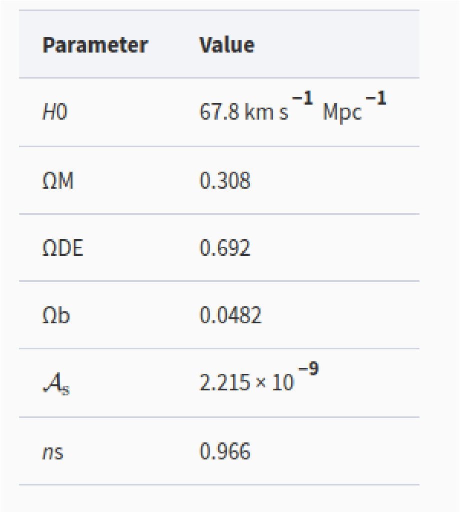

Parameter	Value
$H0$	67.8 km s^{-1} Mpc^{-1}
ΩM	0.308
ΩDE	0.692
Ωb	0.0482
$\mathcal{A}_s$	2.215×10^{-9}
ns	0.966

Figure 3.1: The set of cosmological parameters from the Planck mission [1]. The subscript M indicates the whole matter component (DM + baryons), and the subscript b indicates the baryonic component. The last two variables are the spectral index of the primordial density perturbations and the its amplitude respectively. Image from Baldi and Simpson [3].

while for CDM particles a drag term associated with the interaction with DE causes a different behaviour.

Therefore, the inclusion of baryons provides the possibility of looking at the relative distribution of the two fluids which is likely to show the effect of the different dynamics and thus lead to possible observational features.

Cosmological parameter are based on the latest Planck mission [1] and are summarised in **Figure 3.1**.

With our halo catalogues at hand we have computed the formation of structures, whose main results will be shown in Chapter 4. Some properties such as the nonlinear power spectrum, the gravitational bias, and the halo mass functions have been already analysed in recent papers, here we focus on the effect of coupling on the formation of dark matter halos, namely how the extra friction/drag force impacts on their density and velocity profiles.

Baldi and Simpson [3, 4] extracted the nonlinear matter power spectrum of the two constant-w (**Figure 3.2**) and the two variable-w (**Figure 3.3**) models from the simulations for three different redshifts $z = 0$, $z = 0.5$, and $z = 1$.

The former image shows that on linear scales, for $w = -1.1$ models the power is enhanced, while if $w = -0.9$ it is suppressed, at all redshifts with a deviation varying from $\simeq 8\%$ to $\simeq 12\%$ according to z. The effect appears to be reversed on nonlinear scales, as $w = -0.9$ provides an enhancement of the nonlinear power and $w = -1.1$ causes a suppression of it.

The second image shows the ratio of the nonlinear power spectrum of all the models of our interest. Clearly, it is more complicated to study the effects of the variable-w cosmologies than the constant-w cases, as w evolves in time. In general, HYP and CPL seem to have a minor impact at small scales with respect to the wCDM models. A mild effect as such is preferable since we are looking

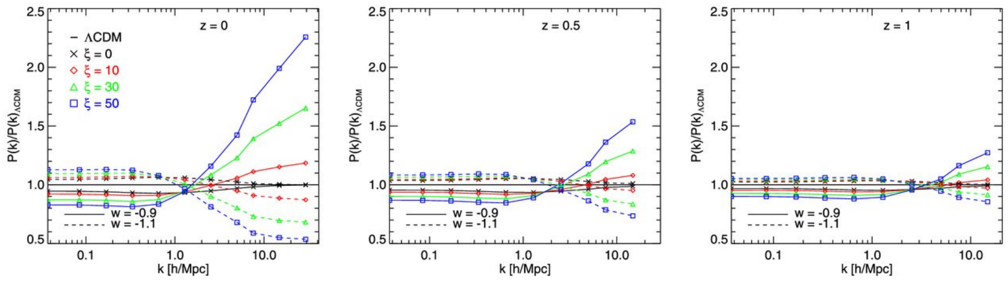

Figure 3.2: The ratio of nonlinear power spectrum of the wCDM models compared to the standard ΛCDM for three redshifts $z = 0$, $z = 0.5$, and $z = 1$. It can be noticed that at large scales there is a scale-independent suppression for $w = -0.9$ and an enhancement for $w = -1.1$, while at small scales the effect is reversed and scale-dependent. One can see the transition between the two regimes. Image from Baldi and Simpson [3].

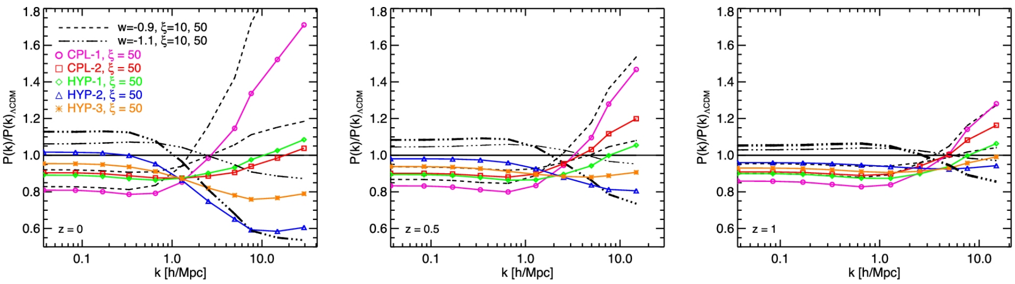

Figure 3.3: The ratio of nonlinear power spectrum of the five models ΛCDM, HYP, CPL, and the to wCDM models. Image from Baldi and Simpson [4].

for a parametrisation able to provide a suppression of structure formation, while maintaining the inner properties of the halos.

Figure 3.4 displays a snapshot of the N-body simulation under investigation at $z = 0$, within a 200 Mpc/h box. The three models ΛCDM, HYP, and CPL are shown. Filamentary structures and cluster clustering appear well resolved, and we can also see the largest structures formed (i.e. massive cluster halos).

It can be noticed even with a visual inspection that the two variable-w models have a mild different evolution of density perturbations with respect to the standard ΛCDM model, while the global shape of the large-scale cosmic web is common, which is not surprising given the same initial conditions.

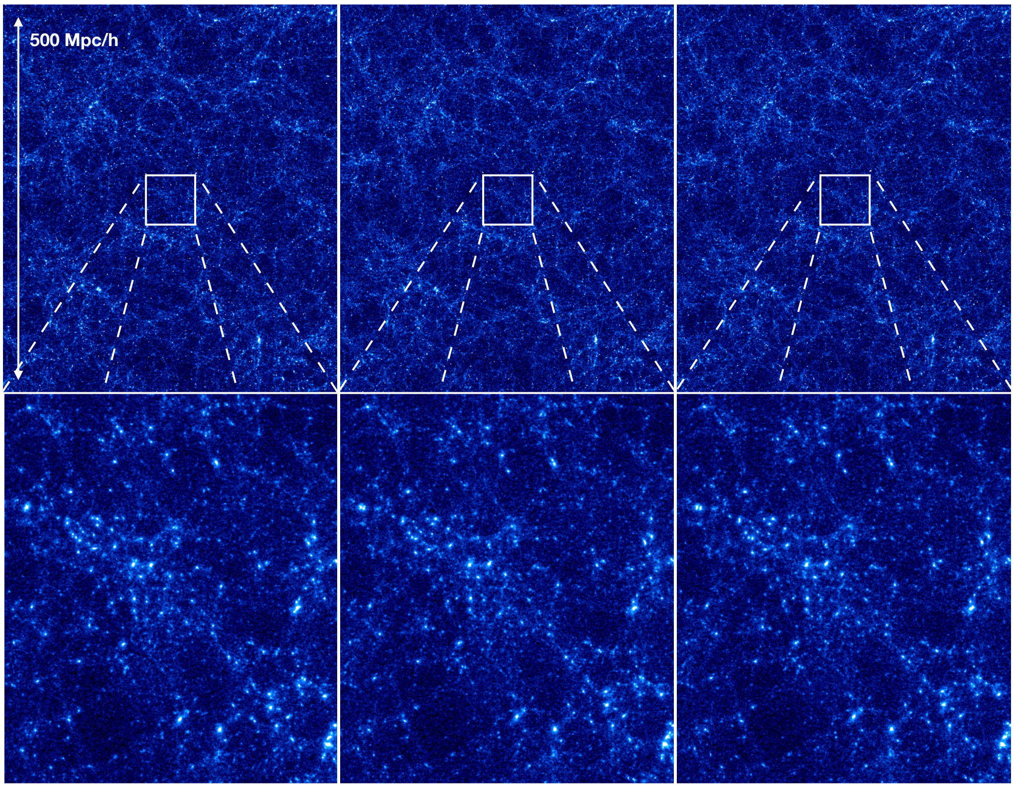

Figure 3.4: Snapshots at $z = 0$ for three models ΛCDM, HYP, and CPL.

Chapter 4

Post-processing

Now we focus on the main results obtained from the data analysis of simulations seen in the previous chapter. The main goal of this project thesis is to study how different models can impact on structure formation, in particular we want to see what happens to the density and velocity profiles of halos in the context of the dark scattering cosmologies described in Chapter 2. In order to better understand the effects of a drag/friction term on the accretion of matter into the potential wells as a function of time we have considered three redshifts $z = 0$, $z = 0.5$, and $z = 1$, and three mass bins to underline the differences among cluster halos, group halos and galaxy halos.

Both density and velocity profiles are studied over the same mass bins, which only vary with z (and this is understandable since halos have different masses as they evolve).

The results of the study consist in a series of plots showing density and, for the first time on these data, velocity profiles of a significant number of randomly selected Dark Matter halos for each cosmology and each mass bin, for a total of 36 computed profiles.

4.1 Density Profiles

In the last decades simulations have reached resolutions so high that density profiles of dark matter halos could be described with reliable accuracy. In particular, it has been demonstrated that relaxed dark matter halos exhibit a density profile characterized by a double power law, with outer asymptotic slope close to -3 and inner asymptotic slope of around -1 (Navarro, Frenk, and White [17, 18])

$$\rho(r) \propto \frac{1}{r\left(1+\frac{r}{r_s}\right)^2}. \tag{4.1.1}$$

Profiles described by 4.1.1 are singular and change shape at a certain scale r_s. The remarkable aspects about the NFW profile are the facts that it is a result that first came out from simulations, and simulated halos proved to be well described by this 'universal' suitably rescaled profile, independent of the halo mass. This drove scientists to put many efforts in providing a theoretical explanation for it.

From our simulated data we took 150 randomly selected halos for every mass bin and model. Then the density distribution is computed by dividing the halo radius into logarithmically equispaced radial bins from a minimum radius to a maximum radius. We counted the number of DM particles lying in every distance bin, and given that all particles have the same mass, thanks to this calculus we were able to compute the value of density as a function of the distance from the centre.

The minimum and maximum radii are chosen to be $r_{\rm min} = 0.1R_{200}$ and $r_{\rm max} = 2R_{200}$, where R_{200} is defined as the radius at which the density of the halo is 200 times the critical density $\rho_{\rm crit}$ (see Chapter 1).

R_{200} is a property of each halo and varies according to the redshift and halo mass. For example, at $z = 0$ R_{200} has values around 10^{5-6} pc for the most massive halos, while it has a order of magnitude lower value for smaller halos and at higher z. The virial mass follows from R_{200}

$$M_{200} = \frac{4}{3}\pi R_{200}^3 200\rho_{crit} \tag{4.1.2}$$

Density profiles of models under investigation are illustrated in **Figure 4.1**, **Figure 4.2**, and **Figure 4.3**, divided into three sets of plots according to the chosen mass bins. Left panels provide all ΛCDM halo profiles (in red) and their stacked profiles (in black). The latter is used as a reference model in right panels (in black), which also display density profiles for the two variable-w cosmologies HYP (in red) and CPL (in green). For a formal description of the two models see Chapter 2.

Vertical lines in the graphs represent the virial radius, which is often considered to be the edge of a halo and here it is taken to be coincident to R_{200}.

At $z = 0$ (**Figure 4.1**), the three mass bins are $6 \cdot 10^{13} < M/M\odot < 2 \cdot 10^{14}$ (galaxy-halos), $2 \cdot 10^{14} < M/M\odot < 6 \cdot 10^{14}$ (group-halos), $6 \cdot 10^{14} < M/M\odot < 3 \cdot 10^{15}$ (cluster-halos).

In **Figure 4.2**, density profiles of halos at $z = 0.5$ are shown. Here, the mass bins taken are $10^{13} < M/M\odot < 7 \cdot 10^{13}$ (galaxy-halos), $7 \cdot 10^{13} < M/M\odot < 4 \cdot 10^{14}$ (group-halos), $4 \cdot 10^{14} < M/M\odot < 2 \cdot 10^{15}$ (cluster-halos).

Figure 4.3 illustrates halo density profiles at $z = 1$, for the three mass bins $7 \cdot 10^{12} < M/M\odot < 4 \cdot 10^{13}$ (galaxy-halos), $4 \cdot 10^{13} < M/M\odot < 10^{14}$ (group-halos), $10^{14} < M/M\odot < 7 \cdot 10^{14}$ (cluster-halos).

This change of mass bins is not surprising because we have seen at the end of Chapter 1 that the growth of perturbations follow a specific law and at high z structures are smaller than at $z = 0$.

It appears clear that all cosmologies show a good agreement with the NFW profile, despite the presence of differences around 10% at medium scales that are probably due to statistic uncertainties. Smaller halos seem to depart more from NFW, but again we are positive that these differences stem from the poorer statistic resolution given the lower number of particles.

On the other hand, near to the centre the three models show stronger differences, and we suspect that the problems at the centre are due to poor resolution close to the gravitational softening of the simulations. In fact, we point out that a discrepancy as such is also present in the standard ΛCDM plots.

Given the very small differences between models, we are showing in these plots only the two variable-w and the reference ΛCDM. For completeness, in **Figure 4.4** density profiles of the most massive halos for all five models (ΛCDM,

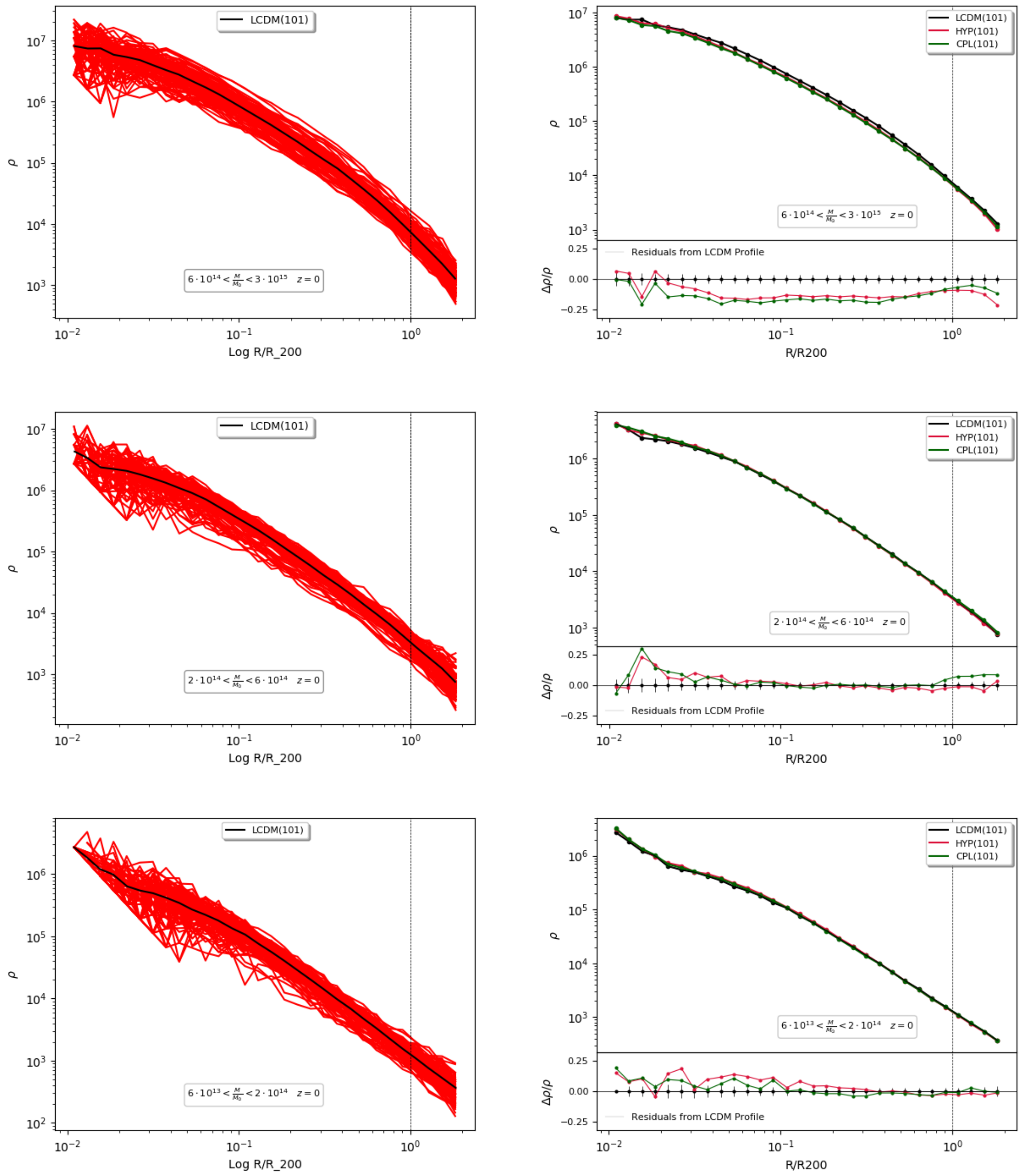

Figure 4.1: Density profiles of dark matter halos at $z = 0$. In left panels all the 100 ΛCDM halos are plotted (in red), and the stacked profile (in black) which is used as a reference model in the right panels.

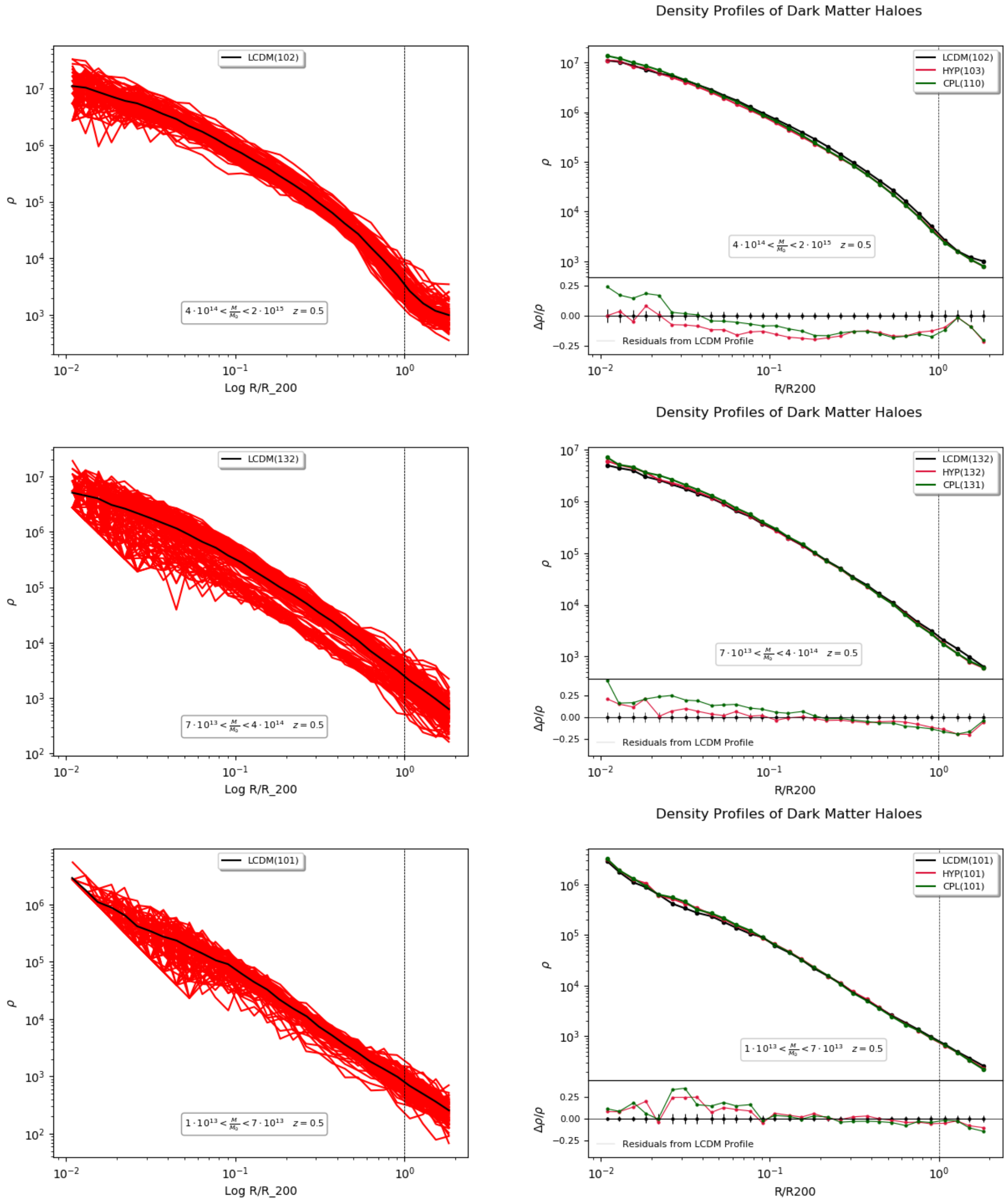

Figure 4.2: Density profiles of dark matter halos at $z = 0.5$. In left panels all the 100 ΛCDM halos are plotted (in red), and the stacked profile (in black) which is used as a reference model in the right panels.

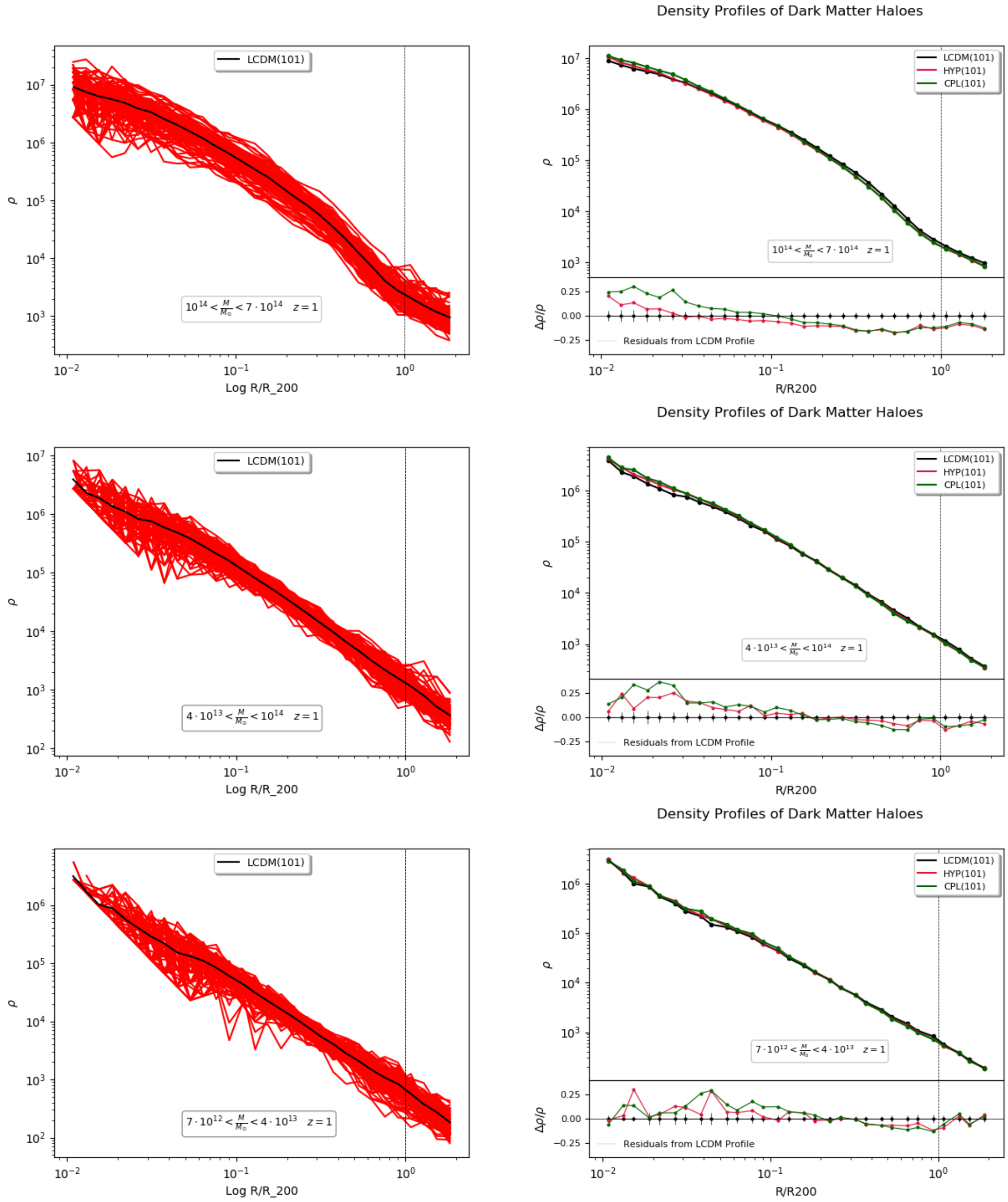

Figure 4.3: Density profiles of dark matter halos at $z = 1$. In left panels all the 100 ΛCDM halos are plotted (in red), and the stacked profile (in black) which is used as a reference model in the right panels.

HYP, CPL, $w\Lambda$CDM) at $z = 0$ are shown. The two $w\Lambda$CDM provide useful insights as their predictions are easier to investigate, because they feature a constant equation of state so that their effects on structure formation only depend on a constant effective friction or drag. In fact, we have seen in Chapter 2 that if $w = -1.1$, the scattering between DE and DM causes an enhancement of structure formation on large scales and a suppression on small scales, and viceversa for $w = -0.9$. The radius at which the inversion of trend takes place should correspond to the transition from linear to nonlinear regime.

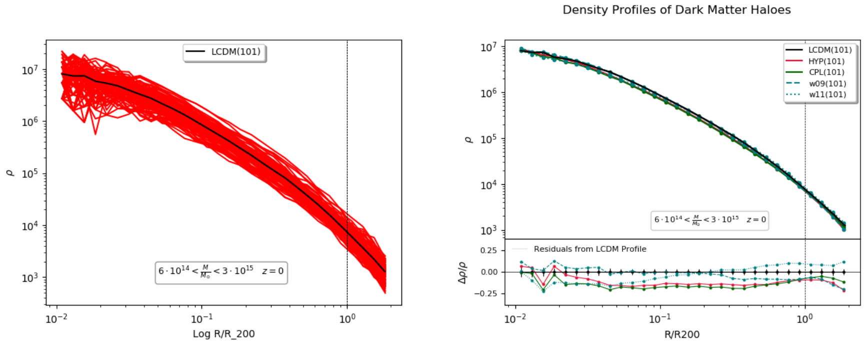

Figure 4.4: Density profiles of dark matter halos at $z = 0$. In left panel all the 150 ΛCDM halos are plotted (in red), and the stacked profile (in black) which is used as a reference model in the right panel). Here only the most massive halos are showed (corresponding to $6 \cdot 10^{14} < M/M\odot < 3 \cdot 10^{15}$). Right panel shows ΛCDM (in black), HYP (in red), CPL (in green), $w = -0.9$ model (dashed blue line), and $w = -1.1$ model (dotted blue line).

4.2 Velocity Profiles

As for the velocity profiles, we modified the program used for the density profiles so that it could extrapolate the cartesian components of velocity for every particle in each bin, and then we computed the velocity module. After that we derived the radial and tangential velocities as the projection of velocity along the direction of motion and perpendicular to it respectively.

Since mass is an extensive quantity, in the previous section we could sum all masses of particles to obtain the density profiles, now we have to take the mean velocity for each bin instead, being velocity an intensive quantity.

We analyse separately these three components in order to carry out a more comprehensive study on the effects of different cosmologies. The mass bins are the same used for the density profiles for the three redshifts $z = 0$, $z = 0.5$, and $z = 1$, and for a better investigation all models are plotted.

4.2.1 Velocity Module

In **Figure 4.5** velocity profiles at $z = 0$ for the five models ΛCDM, HYP, CPL, and the two constant-w are shown. As we expected, bigger halos feature a clear suppression of velocity for HYP, CPL, and $w = -0.9$. This is due to the friction term arising from the scattering between dark energy and dark matter, which acts as a friction term on particles falling into the potential wells of halos, resulting in lower value of velocities for these models.

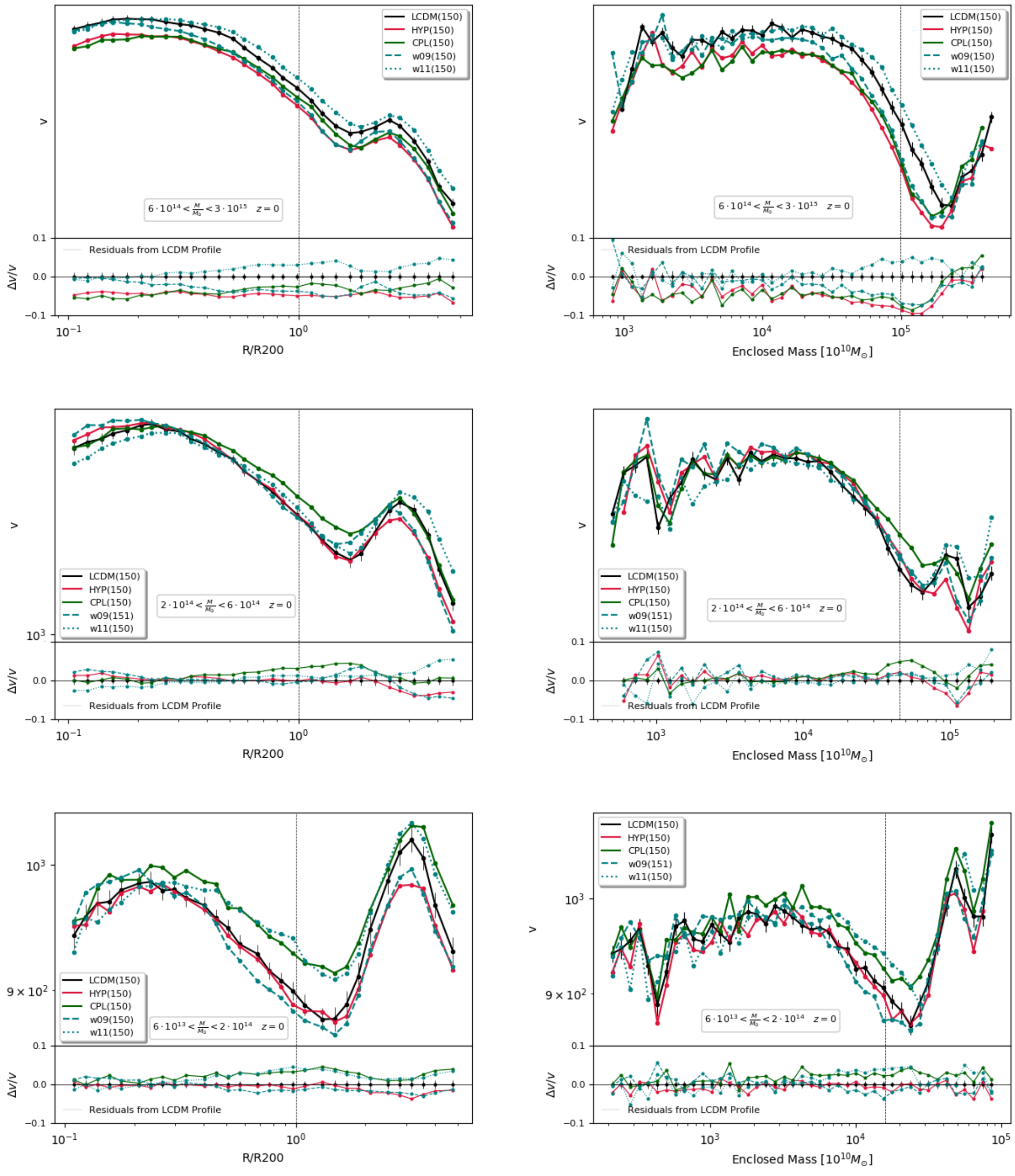

Figure 4.5: Velocity profiles of dark matter halos at $z = 0$. Left panels show the mean velocity of particle as a function of radius, in right panels how it varies according to the included mass inside the halos.

In dark scattering models, the friction term takes the form (see 2.3.3)

$$A \propto 1 + w_{\mathrm{DE}},$$

so that for $w < -1$, A is negative and acts like a drag.

Models show little differences in their profile shapes: $w = -0.9$ is similar to ΛCDM in the central parts and suppress velocities in the outer regions, while the two variable-w models suppress velocities at all scales. This is even more evident in the plots with enclosed masses (right panels in the figures), which show all these three models being permanently below ΛCDM, while $w = -1.1$ is similar to the standard model in the central region and above it in the external parts.

The way particles fall into the forming halos is responsible for this kind of behaviour. In fact, at sufficient distances from the centre the radial infall is enhanced or suppressed by this friction term A, until particles start to rotate and their motions gain a tangential component. When this happens, the effects of dark scattering are more complex to analyse.

On the other hand, by looking at smaller halos one can notice how this effect is reversed for the CPL model, which shows an enhancement in velocities around the virial radius, and it is even stronger in group and galaxy halos.

The cause of this apparent anomaly lies in the evolution of w according to the model. In Chapter 2 we introduced all the models under investigation, and the Chevallier-Polarski-Linder (CPL) has the form

$$w_{\mathrm{CPL}}(a) = w_0 + (1 - a)w_a,$$

where w is a linear function of the scale factor a, w_a indicates the low-z evolution of w_{CPL}; w_0 is the value of w at present time, while at high z it is equal to $w_0 + w_a$. Baldi and Simpson [4] demonstrated that the evolution of w_{CPL} is in the form of a curve with negative convexity, and around $z = 0.5$ it starts to assume < -1 values (**Figure 2.1**, red line).

We already know that $w = -1$ is a critical threshold, because it determines opposite effects on structure formation for models with constant $w < -1$ and models with constant $w > -1$. For this reason, while at high redshifts w_{CPL} has always $w > -1$ values, so that its impact is similar to the one caused by HYP and $w = -0.9$ cosmologies, when w_{CPL} becomes < -1 the result is a drag-like term acting in the direction of an accelerated infall.

The fact that this effect on CPL parametrisations is present only in less massive halos is non trivial. It can be ascribed to the different importance that this kinetic term has with respect to the potential term: in bigger halos, the potential wells are deeper so that the effect is not relevant, while in smaller halos it is more significant and causes an observational signature.

Another evidence of this behaviour can be noticed by looking at the resulting velocity profiles at $z = 0.5$ and $z = 1$ (**Figure 4.6** and **Figure 4.7**). Bottom panels of both images show a considerably high level of statistic uncertainties, which are larger in these plots as the masses taken into account are far smaller with respect to the $z = 0$ case. Resolution is therefore poorer given the fact that there are fewer particles in these halos. It is better to focus on bigger halos: all models stay well below ΛCDM, with the exception of the $w = -1.1$ parametrisation which show an enhancement in velocity values as expected.

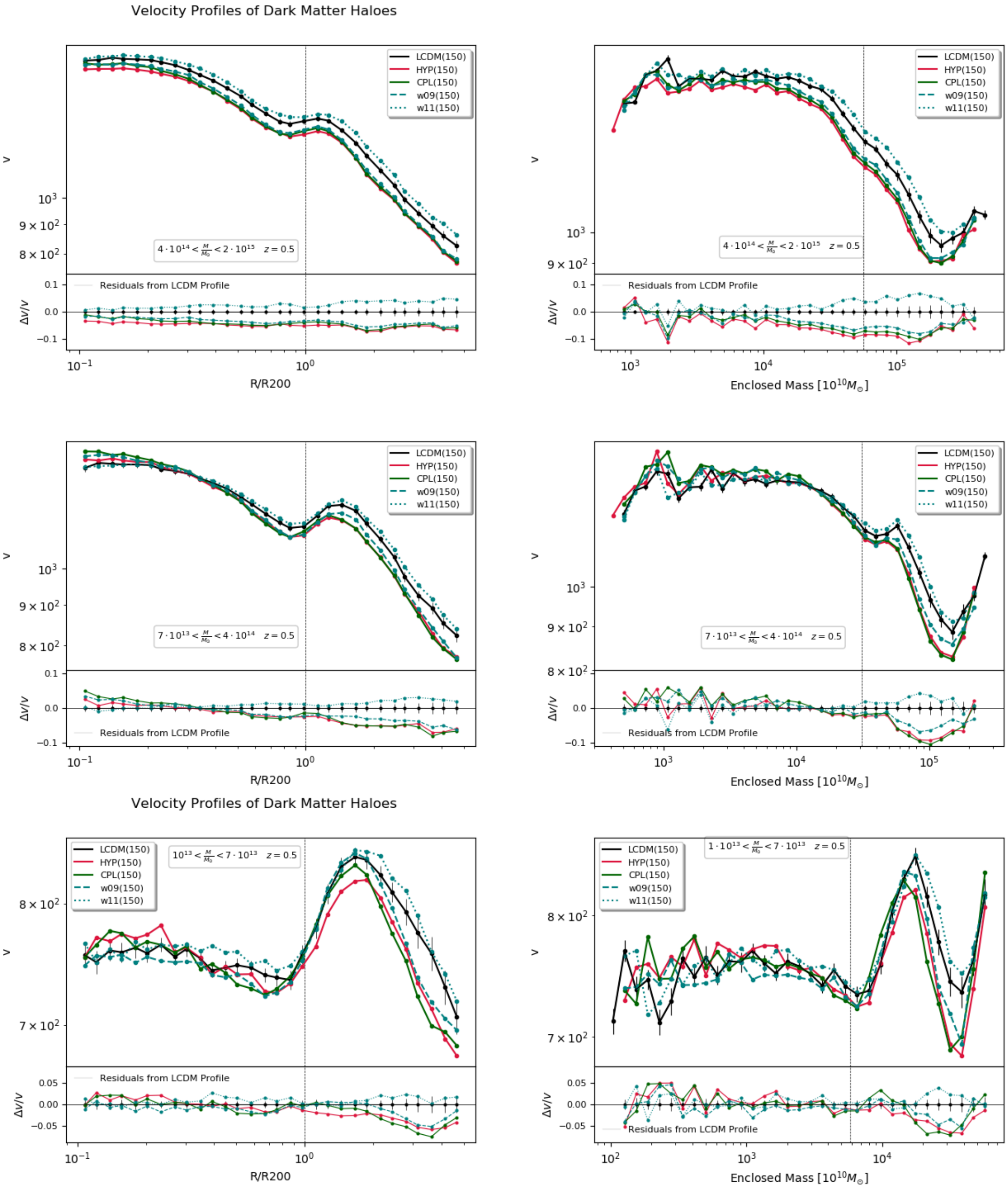

Figure 4.6: Velocity profiles of dark matter halos at $z = 0.5$. Left panels show the mean velocity of particle as a function of radius, in right panels how it varies according to the included mass inside the halos.

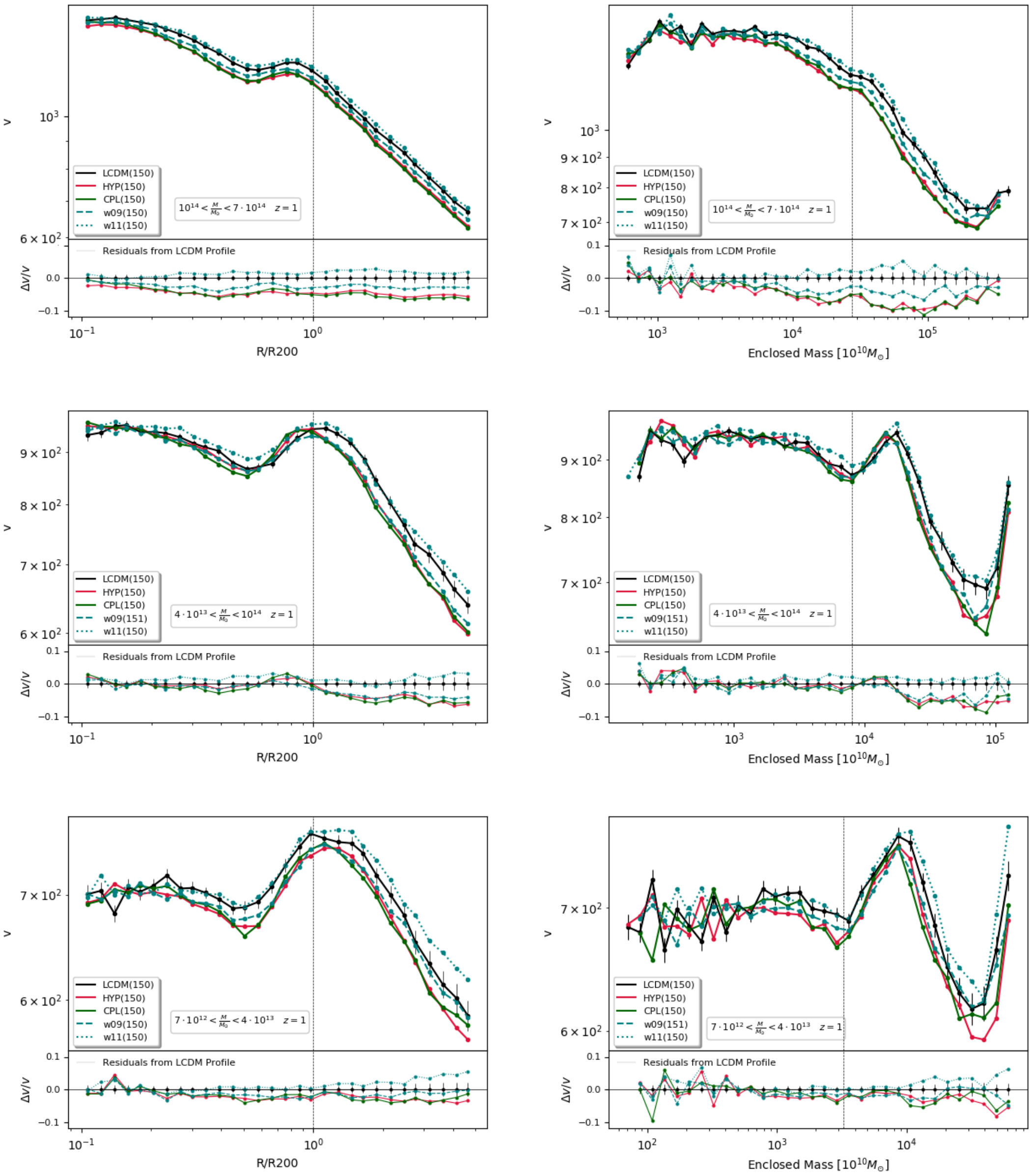

Figure 4.7: Velocity profiles of dark matter halos at $z = 1$. Left panels show the mean velocity of particle as a function of radius, in right panels how it varies according to the included mass inside the halos.

4.2.2 Radial velocities

Once the velocity of a particle is derived, its radial component is obtained by the projection of v along the radius between the particle and the centre of the halo, so that radial velocity is the particle's velocity towards the centre of the halo.

Radial velocity profiles usually have a maximum value at some intermediate radius and decrease both towards the centre and towards the outskirts. This peak in the curves is known as the *turn-around radius*, as it separates two distinct regions. At sufficient distance from the halo, a particle moving in the Hubble flow starts to being attracted by the gravitational field of the well and its velocity increases in the direction of it.

To find the turn-around in non trivial, as there are several processes within the halo that could modify and perturb the trajectory of a particle. A visual idea of what happens can be seen through two examples illustrated in **Figure 4.8** and **Figure 4.9**, which show two $z = 0$ radial velocity profiles of massive halos simulated with ΛCDM model.

The shape of the first curve is well defined, and one can easily see where the particles reach the minimum in velocity after being slowed down during the Hubble flow, which corresponds to the turn-around radius (golden dot in the image). A halo as such is likely to be isolated and quite homogeneous (i.e. the substructures within are absent or small).

Conversely, the second plot appears to be considerably perturbed, the Hubble flow is hard to detect, and thus it presents various minima and maxima (red dots in the images). This is due to the presence of substructures inside the halo which perturb the halo itself and the particles falling into it. If the halo is not isolated (namely if it is close to a DM filament) the profile will appear unstable as well. These halos could provide an incorrect measurement of the turn-around radius if one simply take the global minimum of the curve. In order to overcome the problem, we took the maximum of the function (pink dots in the images) and looked for the closest minimum to it which didn't have a lower point near to it.

When a particle enters in a region completely dominated by the collapse (i.e. after passing the turn-around radius), the virialization process makes the particle gain a tangential velocity which lower the value of the radial component. Thereby, infalling particles stabilise their orbits around the centre of the well and virial equilibrium is reached.

Clearly, the effect of dark scattering is more significant for this component of velocity, as it acts as a drag/friction directly on the radial velocities of particles, at least in linear regime.

Models featuring a scattering between DM and DE have an opposite impact on infalling matter. At linear regimes, particles are far from the centre of the halo and the friction (drag) term acts in the direction of motion slowing down (accelerating) them. When particles start to convert their radial velocity into tangential velocity, namely when the virialization process begins, this extra friction (drag) is no longer parallel to the motion, and it enhances (decrease) the loss of kinetic energy, thus resulting in a faster (slower) virialization.

For this reason, halos simulated with CPL, HYP, and $w = -0.9$ cosmologies are supposed to form earlier.

In **Figure 4.10**, radial velocity profiles for simulated DM halos at $z = 0$

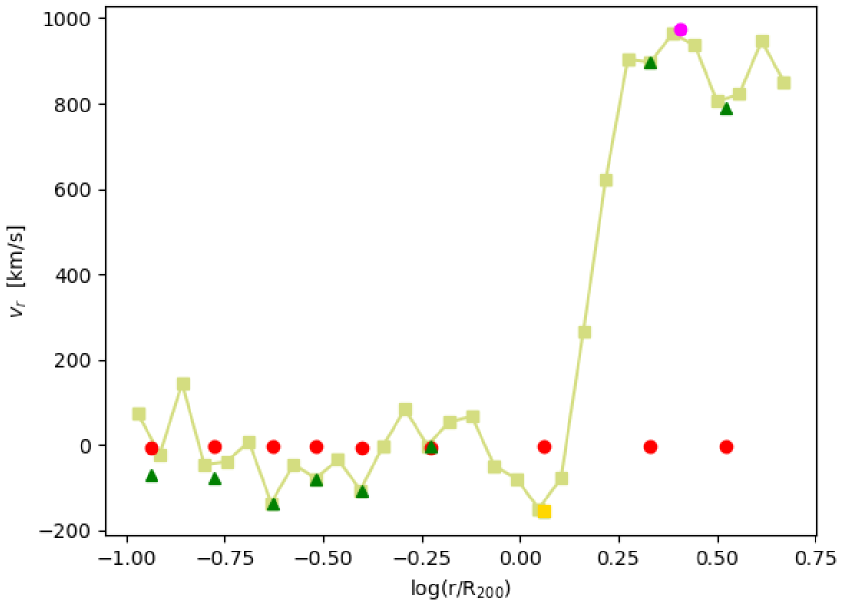

Figure 4.8: Radial velocity profile of a dark matter halo at $z = 0$. Red points represent the projected minima of the curve, the turn-around radius is indicated with the golden point.

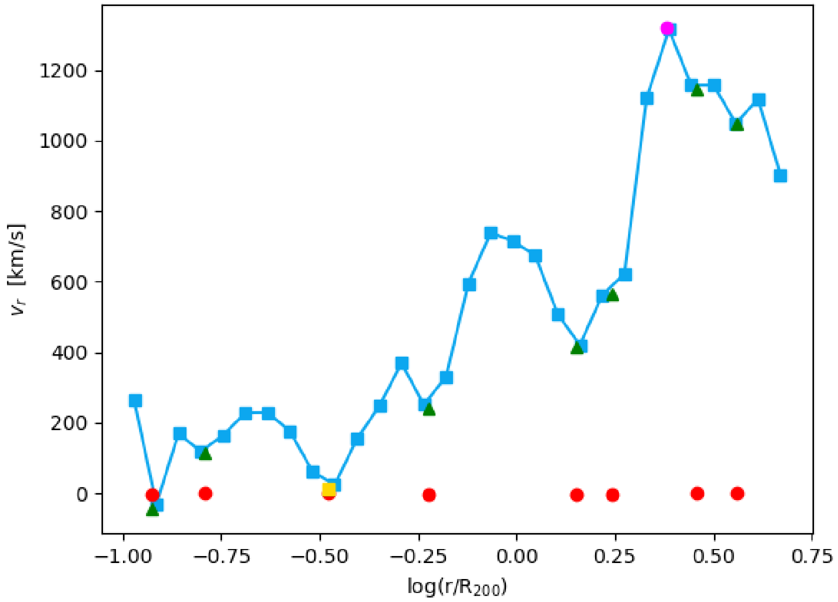

Figure 4.9: Radial velocity profile of a dark matter halo at $z = 0$. Red points represent the projected minima of the curve, the turn-around radius is indicated with the golden point.

are shown. We can see that all models follow the same shape, and for massive halos they are very similar to the reference ΛCDM at large radii, while they remain below it inside the turn-around radius, except for the $w = -1.1$ whose behaviour is coherent with respect to our predictions discussed before.

Conversely, less massive halos provide a weaker signal and the plots are more scattered, especially the ones with enclosed mass near to the centre.

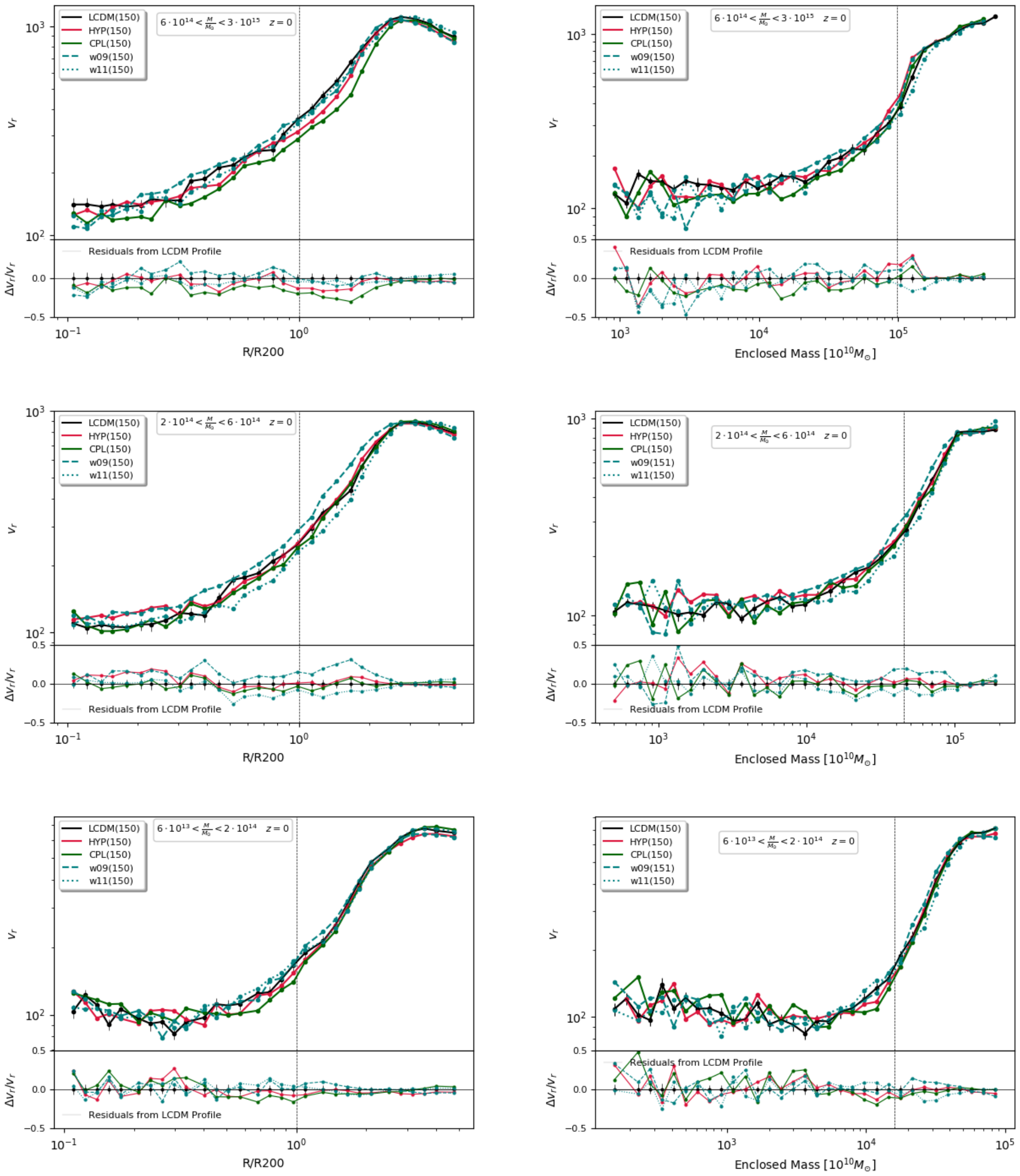

Figure 4.10: Radial velocity profiles of dark matter halos at $z = 0$. Left panels show the mean velocity of particle as a function of radius, in right panels how it varies according to the included mass inside the halos.

If we look at higher z, the effect on small scales is still present, while the global shape appears steeper than the $z = 0$ profiles.

In **Figure 4.11**, HYP and CPL profiles exhibit a shift in the turn-around radius towards smaller scales, as it can be noticed in plots with enclosed mass.

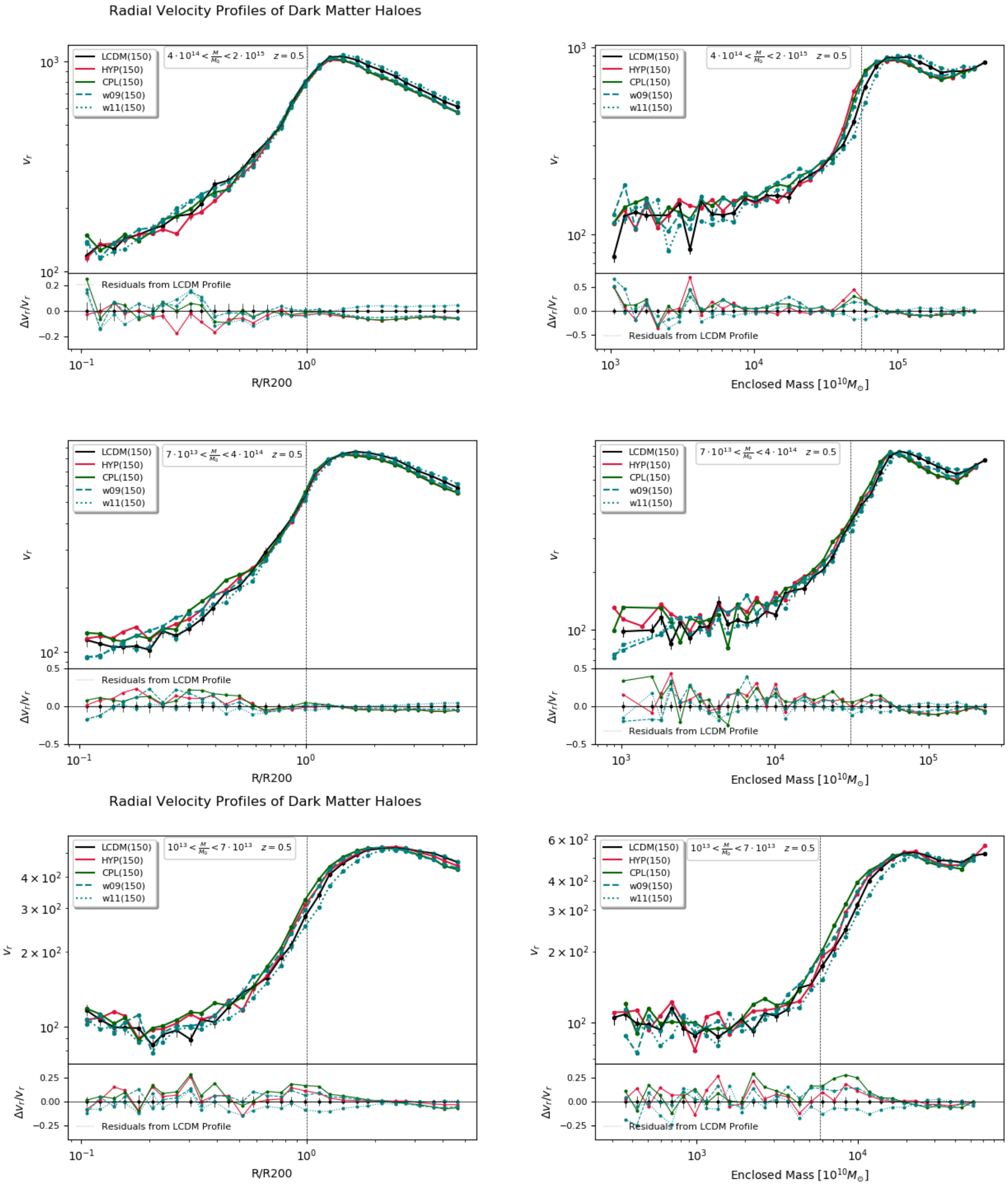

Figure 4.11: Radial velocity profiles of dark matter halos at $z = 0.5$. Left panels show the mean velocity of particle as a function of radius, in right panels how it varies according to the included mass inside the halos.

This effect appears to be more significant at $z = 1$ (**Figure 4.12**).

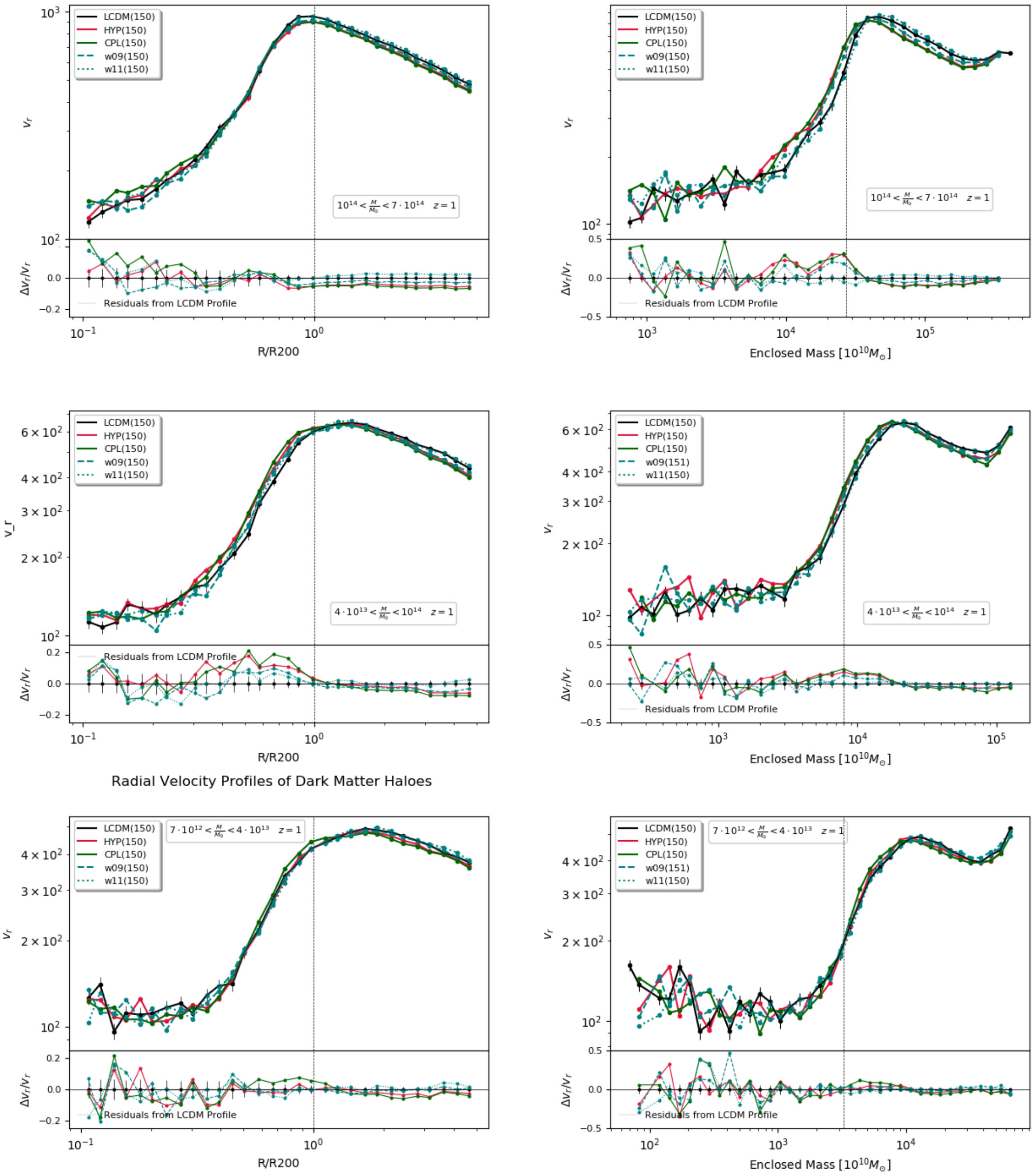

Figure 4.12: Velocity profiles of dark matter halos at $z = 1$. Left panels show the mean velocity of particle as a function of radius, in right panels how it varies according to the included mass inside the halos.

4.2.3 Tangential velocities

Global shapes of tangential velocity profiles are in good agreement with what we discussed in the previous sections (**Figure 4.13**, **Figure 4.14**, and **Figure 4.15**). In fact, at the turn-around radius particles reach the maximum infall velocity before being slowed down by the onset of virialization. As a consequence, tangential component of velocity increases towards the halo centre.

We can see that a lower resolution is present also in these plots, which makes higher mass profiles more reliable.

At $z = 0$, $w = -1.1$ model is always above ΛCDM, while the others stay below it with slightly different shapes. The graphs with enclosed mass provide a small signal at small scales, while the separation between models appears clear around R_{200}, where velocity fields are different for equal enclosed masses. The effect on the CPL model seen in total velocity plots is here evident for small halos.

This effect ceases to exist at $z > 0$, which is in agreement with what we discussed in the previous section.

4.3 Statistical insights

In order to derive the stacked profiles for both r/R_{200} and enclosed mass, for each cosmology we took the values needed from the output halos data, then we listed all radii, densities, masses, and velocities into 4 single arrays.

We used a histogram-like algorithm to divide these arrays into equispaced bins: for the x-axis variables (radius and mass) we computed the mean value of each bin, while we considered the y-axis variables (density and velocity) as weights, namely each value in the x-array only contributes its associated weight (i.e. the corresponding density or velocity) towards the bin count (instead of 1). This way, for every x bin we obtained the sum over the y values, from which we derived the mean.

Error bars are computed as the standard deviations on the mean values of the reference profile (i.e. the ΛCDM), using the formula

$$\sigma_y = \frac{1}{\sqrt{N}} \sqrt{\frac{1}{N} \sum_i^N (y_i - \bar{y})^2}, \tag{4.3.1}$$

where $\bar{y}$ is the mean of the data

$$\bar{y} = \frac{1}{N} \sum_i^N y_i. \tag{4.3.2}$$

In the scatter plots, error bars on the ΛCDM curves are obtained by dividing σ_y by $\bar{y}$.

The whole set of plots seen so far was analysed by this statistical approach. For a higher precision study, resampling techniques were used as well.

The *Jackknife* estimator relies on the omission of a percentage of the dataset. The estimate of a parameter is thus found by computing the estimate from the subsample and then finding the mean of these calculations. For instance, a simple jackknife estimate of the mean of a population can be obtained by taking n estimates of $\bar{x}$ over a set of subsamples that comprise all but the i-th point

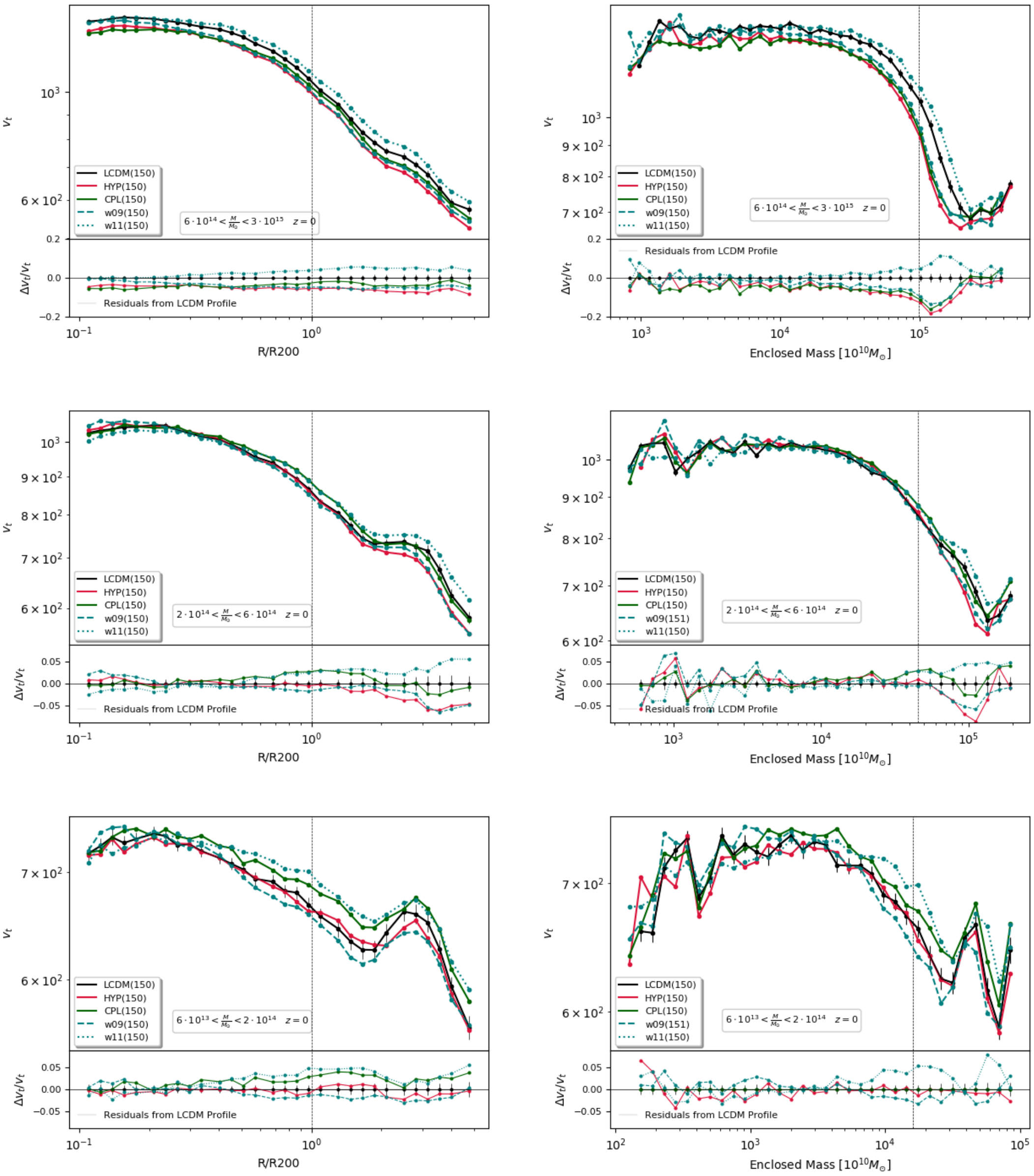

Figure 4.13: Tangential velocity profiles of dark matter halos at $z = 0$. Left panels show the mean velocity of particle as a function of radius, in right panels how it varies according to the included mass inside the halos.

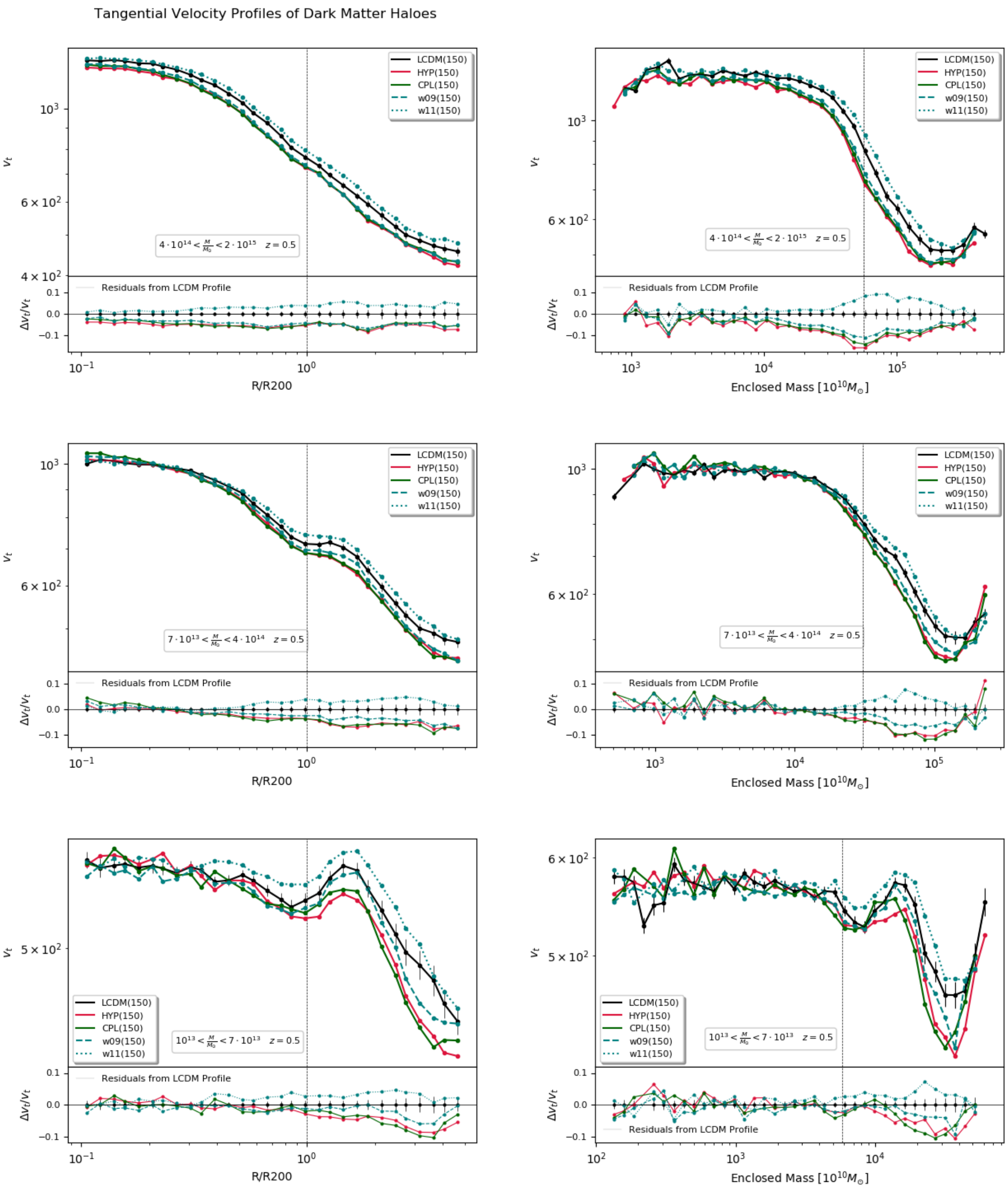

Figure 4.14: Tangential velocity profiles of dark matter halos at $z = 0.5$. Left panels show the mean velocity of particle as a function of radius, in right panels how it varies according to the included mass inside the halos.

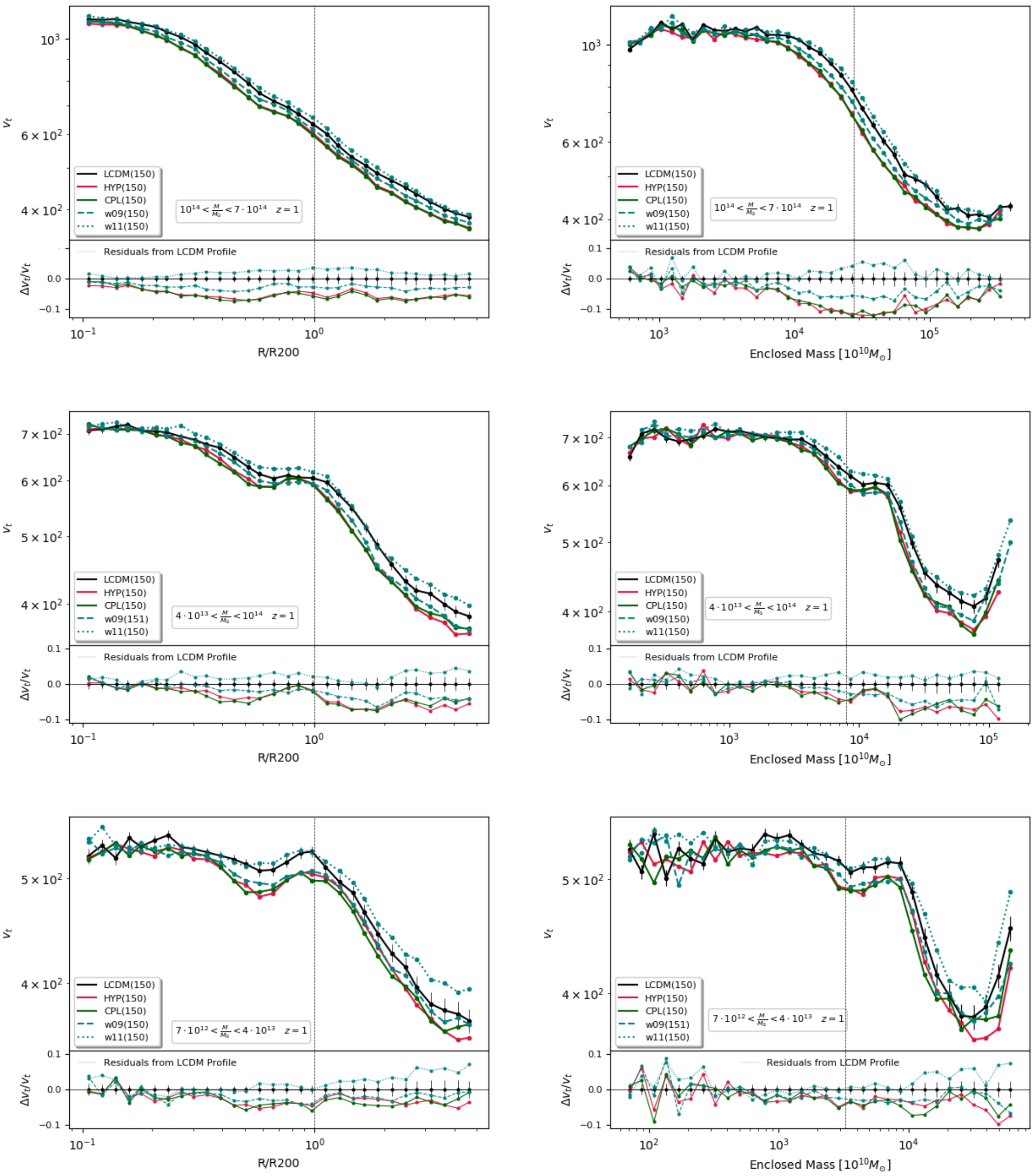

Figure 4.15: Tangential velocity profiles of dark matter halos at $z = 1$. Left panels show the mean velocity of particle as a function of radius, in right panels how it varies according to the included mass inside the halos.

$$\bar{x}_i = \frac{1}{n-1}\sum_{j\neq i}^{n} x_j,$$

so that the population mean is the average of these n estimates

$$\bar{x} = \frac{1}{n}\sum_{i}^{n} \bar{x}_i.$$

We applied the jackknife technique to our sets of halos by performing 100 estimates of the stacked profiles for 80% randomly selected halos.

The *Boostrap* resampling is based on random sampling with replacement, namely it takes the same number n of variables as the the set, so that each data point can be selected more than once.

Here again, we applied the bootstrap technique to our halo sample by calculating mean and standard deviation for 100 resampled data.

In **Figure 4.16** the results of our efforts are shown. Top panel illustrates the density profile for 101 simulated halos at $z = 0$ in ΛCDM, HYP, and CPL models. Halo masses ranges from $6 \cdot 10^{13}$ to $2 \cdot 10^{14}$ in solar mass units (these profiles are the same to the ones displayed in **Figure 4.1**).

Lower panels show the application to the resampling statistic to the same halos: it can be noticed how there are very small differences between the three plots, so that we can conclude that the simple statistic of (4.3.1) and (4.3.2) should be sufficient to provide accurate outcomes.

A further confirmation of the correctness of our analysis can be found in **Figure 4.17**, which features a boostrapped resampling for the tangential velocity profiles of a set of ΛCDM, HYP, and CPL cluster-halos simulated at $z = 0$. Again, the upper panel shows the same plots of **Figure 4.13**, while the lower panel shows the bootstrap resampling result.

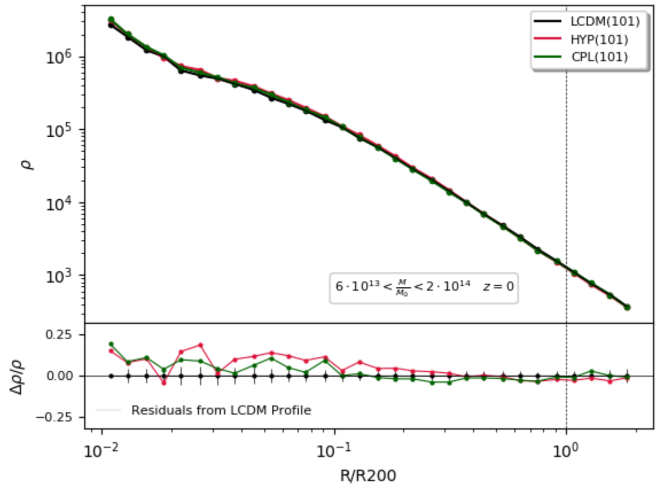

Resampling: jackknife

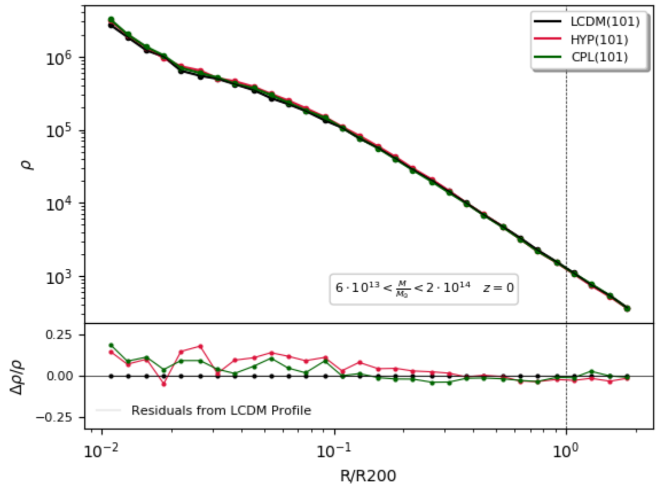

Resampling: bootstrap

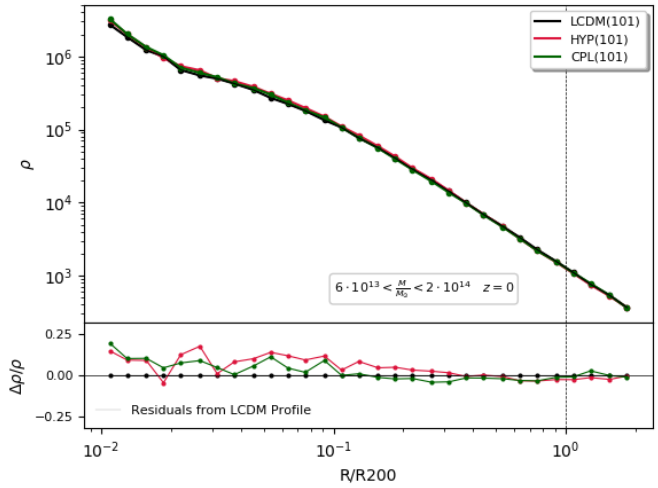

Figure 4.16: Different statistical approaches in the evaluation of density profile to the same set of data (i.e. simulated galaxy-halos in ΛCDM, HYP, and CPL models at $z = 0$)

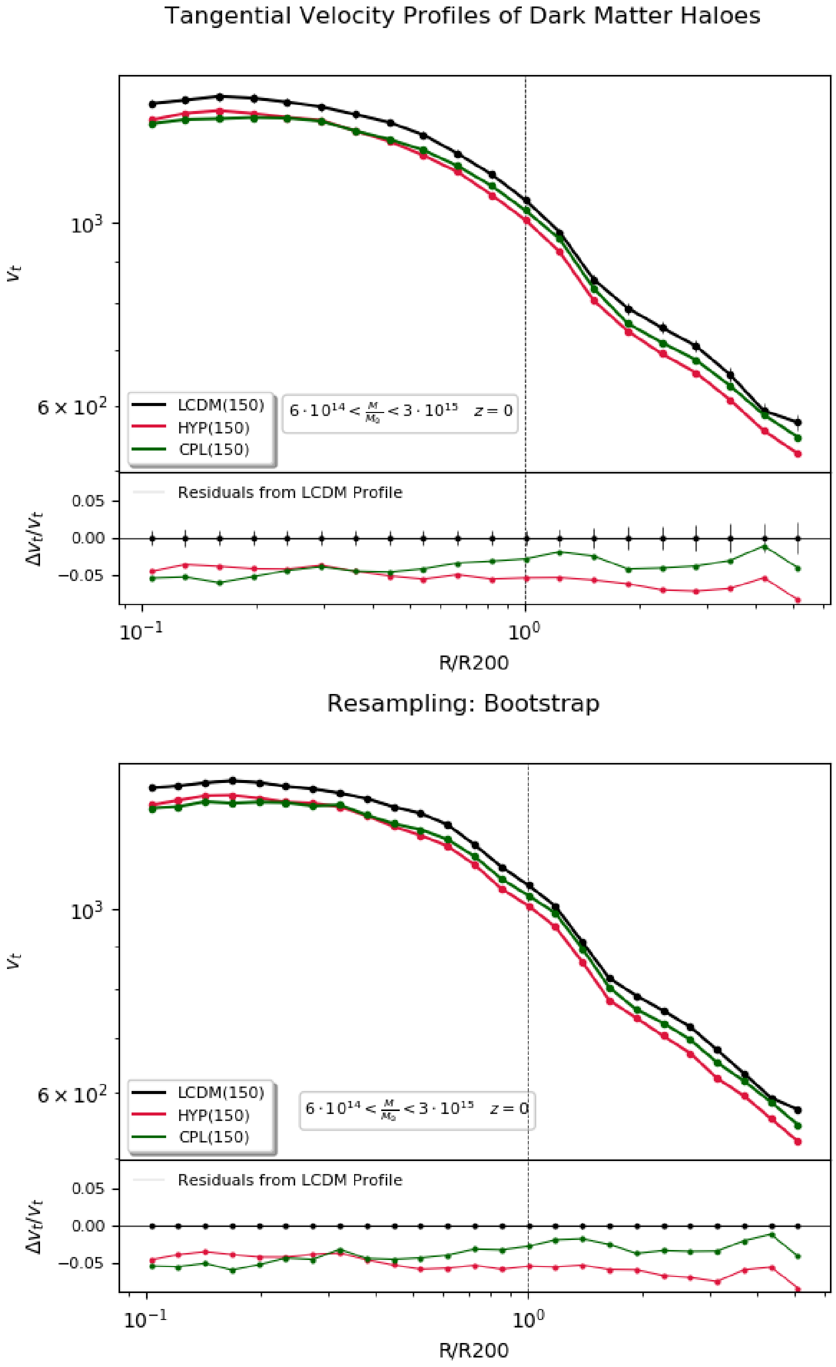
Tangential Velocity Profiles of Dark Matter Haloes

Resampling: Bootstrap

Figure 4.17: Different statistical approaches for the calculus of tangential velocity profiles to the same set of data (i.e. simulated cluster-halos in ΛCDM, HYP, and CPL models at $z = 0$)

Chapter 5

Conclusions

The standard concordance model ΛCDM is remarkably predictive as a model, and it has been tested in a series of observational experiments which checked the accuracy of its parameters. However, it suffers from both theoretical and observational problems.

There are persisting tensions arising from low-redshifts probes such as cluster counts and weak lensing data, which point towards a lower rate of structure growth with respect of the ΛCDM predictions normalised using the CMB data from Planck. A possible explanation of these contrasts is that ΛCDM is not the correct model to describe the properties of the Universe. The search for alternative theories capable of a better fit with the data has led to a plethora of models based on different physical phenomena.

Since the true nature of the two constituents of the dark sector (Dark Energy and Dark Matter) is far from being known, they may feature some kind of interaction, and the fact that they are considered uncoupled is just an assumption. Several models of Coupled Dark Energy have been proposed in the last years; however, the vast majority of them are characterized by an energy-momentum transfer, causing a modification of both the expansion history and growth of structures.

On the other hand, Dark Scattering models only invoke a momentum exchange, as they are based on an elastic scattering between DE and DM. This type of interaction was chosen given the low density associated with DE and the non-relativistic velocities the DM particles are thought to possess. Momentum exchange has the advantage of altering the formation of structures while the cosmic history remains unaltered. In these scenarios, a particle moving through a dark energy fluid experiences a nonzero flux of momentum due to the nonzero scattering cross-section between DE and DM, so that its motion is affected by the interaction. In particular, dark scattering models are expected to modify the collapse and virialisation process of nonlinear structures, resulting in a suppression of the growth of structures in the linear regime, and a faster collapse in the nonlinear regime.

In fact, in the linear regime particles are falling into the potential well of the forming halo with a radial motion, and the DE-DM scattering acts as a friction term slowing down their collapse. In the nonlinear regime, this friction causes a faster loss of kinetic energy of the particles, thus making the halo to contract and reach the virial equilibrium earlier with respect to the uncoupled case.

Dark scattering models have been proved to be a viable alternative theory to the standard cosmological scenario in recent papers [3,4,19], which showed that they can suppress structure growth and reconcile the low-redshift probes with the Planck data. In this project thesis we have extended the work previously carried out with the aim of finding additional observational signatures of the impact of the dark scattering models, which is expected to be significant in the density and velocity profiles of dark matter halos.

In order to analyse these effects, we studied the properties of a number of dark matter halos simulated assuming five different cosmologies: two dark scattering models with a variable equation of state parameter w, two dark scattering models with a constant $w \neq -1$, and a reference ΛCDM model ($w = -1$). We extracted density and velocity profiles of these halos for each cosmology, divided into mass bins considering three different redshifts $z = 0$, $z = 0.5$, and $z = 1$.

The main results can be summarised as follows:

- Density profiles show a good agreement with the NFW profile, with differences between the variable-w models and ΛCDM around 10% at intermediate scales, while the two constant-w provide a clearer behaviour, as $w = -1.1$ ($w = -0.9$) corresponds to an enhancement of structure formation on large (small) scales and a suppression on small (large) scales. The radius at which the inversion takes place indicates the transition from the linear to the nonlinear regime.

- Profiles of the amplitude of velocity provide useful insights on the effects of dark scattering, as bigger halos display a suppression for all cosmologies except for the $w = -1.1$ model, with shows an enhancement of structure formation at all scales. At $z = 0$, one of the variable-w cosmologies shows an opposite effects with respect to what happens at higher redshifts. This is due to the evolution of w in this model, which starts to assume values < -1 at low z so that its impact becomes similar to the one caused by the $w = -1.1$ model.

- Radial velocity profiles have a maximum at some intermediate radius corresponding to the separation between the region dominated by the Hubble flow, in which the particles possess a radial component of motion while being attracted by the halo, and a region dominated by the collapse, where the particles' radial velocity decreases as it gains a tangential component. All models provide the same global shape, and they are similar to ΛCDM at large scales, while remain below it in the inner parts, except for the $w = -1.1$ model whose behaviour is coherent with what we discussed before.

- Tangential velocity profiles are characterized by an increasing slope towards the centre of the halo, due to the onset of the virialisation process which causes the particles to start to rotate and gain a tangential component of velocity. Eventually the particles will have stable orbits around the centre of the halo thereby leading to the virial equilibrium. The two variable-w and the $w = -0.9$ models have profiles always below the ΛCDM profile with slightly different shapes.

Overall, we demonstrated that dark scattering models can provide a suppression of structure formation, and in particular the variable-w parametrisations yield a mild effect on small scales with respect to the two constant-w under investigation, which is preferable since we are interested in models able to cause a suppression of structure formation while maintaining unchanged the inner properties of the halos.

Therefore, density and velocity profiles are two observational probes that could allow us to distinguish between ΛCDM and dark scattering cosmologies, as we saw that they provide different effects on the shapes of the profiles so that they could represent a further signature of the impact of these models.

Bibliography

[1] Planck Collaboration: P. A. R. Ade et al. Planck 2015 results. XIII. Cosmological parameters. *Astronomy & Astrophysics*, 594:A13, September 2016.

[2] Jean-Michel Alimi et al. DEUS Full Observable {\Lambda}CDM Universe Simulation: the numerical challenge. *ArXiv e-prints*, June 2012.

[3] Marco. Baldi and Fergus. Simpson. Simulating momentum exchange in the dark sector. *Mon. Not. Roy. Astron. Soc.*, 449:2239–2249, May 2015.

[4] Marco Baldi and Fergus Simpson. Structure formation simulations with momentum exchange: alleviating tensions between high-redshift and low-redshift cosmological probes. *Mon. Not. Roy. Astron. Soc.*, 465(1):653–666, 2017.

[5] Robert R. Caldwell, Rahul Dave, and Paul J. Steinhardt. Cosmological Imprint of an Energy Component with General Equation of State. *Phys. Rev. Lett.*, 80:1582–1585, February 1998.

[6] Michel Chevallier and David Polarski. Accelerating Universes with Scaling Dark Matter. *Int. J. Mod. Phys.*, 10:213–223, 2001.

[7] Planck collaboration: P. A. R. Ade et al. Planck 2013 results. XX. Cosmology from Sunyaev-Zeldovich cluster counts. *Astronomy & Astrophysics*, 571:A20, November 2014.

[8] Pedro G. Ferreira and Michael Joyce. Cosmology with a primordial scaling field. *Phys. Rev. D*, 58(2):023503, July 1998.

[9] Nick Hand, Graeme E. Addison, Eric Aubourg, et al. Evidence of Galaxy Cluster Motions with the Kinematic Sunyaev-Zel'dovich Effect. *Phys. Rev. D*, 109(4):041101, July 2012.

[10] Stephen Hawking. A Brief History of Time. *Bantam Books*, 1988.

[11] Catherine. Heymans et al. CFHTLenS tomographic weak lensing cosmological parameter constraints: Mitigating the impact of intrinsic galaxy alignments. *Mon. Not. Roy. Astron. Soc.*, 432:2433–2453, July 2013.

[12] Helen Klus. How We Came to Know the Cosmos: Space & Time. 2017.

[13] Michael Kuhlena, Mark Vogelsbergerb, and Raul Anguloc. Numerical simulations of the dark universe: State of the art and the next decade. *Physics of the Dark Universe*, 1:50–93, November 2012.

[14] Eric V. Linder. Exploring the Expansion History of the Universe. *Phys.Rev.Lett.*, 90(9):091301, March 2003.

[15] Chung-Pei Ma and Edmund Bertschinger. Cosmological Perturbation Theory in the Synchronous and Conformal Newtonian Gauges. *Astrophys. J.*, 455:7, December 1995.

[16] Ian Morison. To infinity and beyond. *Gresham College*, 2011.

[17] Julio F. Navarro, Carlos S. Frenk, and Simon D.M. White. The Structure of Cold Dark Matter Halos. *Astrophys. J.*, 462:563, May 1996.

[18] Julio F. Navarro, Carlos S. Frenk, and Simon D.M. White. A Universal Density Profile from Hierarchical Clustering. *Astrophys. J.*, 490:493–508, December 1997.

[19] Alkistis Pourtsidou and Thomas Tram. Reconciling CMB and structure growth measurements with dark energy interactions. *Phys. Rev. D*, 94(4):043518, August 2016.

[20] Bharat Ratra and P. J. E. Peebles. Cosmological consequences of a rolling homogeneous scalar field. *Phys. Rev. D*, 37, 1988.

[21] Adam G. Riess et al. A 2.4% Determination of the Local Value of the Hubble Constant. *Astrophys. J.*, 826:56, July 2016.

[22] Lado Samushia et al. The clustering of galaxies in the SDSS-III DR9 Baryon Oscillation Spectroscopic Survey: testing deviations from Λ and general relativity using anisotropic clustering of galaxies. *Mon. Not. Roy. Astron. Soc.*, 429:1514–1528, February 2013.

[23] Fergus Simpson. Scattering of dark matter and dark energy. *Phys. Rev. D*, 82(8):083505, October 2010.

[24] Kendrick M. Smith and Oliver Zahn. Detection of gravitational lensing in the cosmic microwave background. *Phys. Rev. D*, 76(4):043510, August 2007.

[25] Volker Springel. The cosmological simulation code GADGET-2. *Mon. Not. Roy. Astron. Soc.*, 364:1105–1134, December 2005.

[26] Volker Springel, Carlos S. Frenk, and Simon D.M. White. The large-scale structure of the Universe. *Nature*, 440:1137–1144, April 2006.

[27] Rien van de Weijgaert. Linear Perturbation Theory. 2009.

[28] Frank van den Bosch. Theory of Galaxy Formation. 2009.

[29] Christof Wetterich. Cosmology and the fate of dilatation symmetry. *Nucl. Phys. B*, 302:668–696, June 1988.